

The Hydrostatic Mass Bias and the σ_8 Tension: A Multi-Probe Forecast for Stage-IV/V Surveys

AYODEJI IBITOYE,^{1,2,3} PRABHAKAR TIWARI,¹ QI XIONG,⁴ AND YAN GONG⁴

¹*Department of Physics, Guangdong Technion - Israel Institute of Technology, Shantou, Guangdong 515063, P.R. China*

²*Centre for Space Research, North-West University, Potchefstroom 2520, South Africa*

³*Department of Physics and Electronics, Adekunle Ajasin University, P. M. B. 001, Akungba-Akoko, Ondo State, Nigeria*

⁴*National Astronomical Observatories, Chinese Academy of Sciences,
20A Datun Road, Chaoyang District, Beijing 100101, P. R. China*

ABSTRACT

The hydrostatic mass bias (b_{HSE}) is a leading systematic uncertainty in cluster cosmology and a principal source of degeneracy with σ_8 and Ω_m . We investigate the capability of Stage-IV CMB and optical surveys to calibrate b_{HSE} using tomographic cross-correlations between the thermal Sunyaev-Zeldovich (tSZ) effect, galaxy clustering, and weak lensing. We perform a Fisher forecast incorporating realistic survey noise, foreground modeling for clustered CIB and radio sources, and full marginalization over cosmological and astrophysical nuisance parameters, including per-bin galaxy bias perturbations, photometric redshift shifts, intrinsic alignments, and baryonic feedback modeled with HMCCode2020. With optimized tomographic binning (10 lens and 5 source bins for LSST; 6 lens and 5 source bins for CSST), we forecast marginalized constraints of 0.98% for SO+LSST, 1.60% for CMB-S4+LSST, and 2.40% for CMB-S4+CSST. Tomography improves b_{HSE} precision by factors of approximately three relative to non-tomographic analyses, reflecting the role of redshift information in breaking the $b_{\text{HSE}}-\sigma_8$ degeneracy. Optical-only probes provide no direct constraint on b_{HSE} , whereas inclusion of tSZ-containing spectra enables percent-level calibration under realistic systematic assumptions. The results demonstrate that multi-probe tomographic analyses with Stage-IV surveys can achieve robust control of hydrostatic mass bias, strengthening cluster-based constraints on structure growth.

Keywords: hydrostatic mass bias, tSZ-galaxy cross-correlations, tomography, CMB-S4, LSST, CSST

1. INTRODUCTION

Galaxy clusters, the most massive collapsed structures in the universe, serve as powerful probes of cosmic growth. Their abundance as a function of mass and redshift is exquisitely sensitive to the parameters governing the background cosmology and the growth of structure, most notably the total matter density Ω_m and the amplitude of matter fluctuations, σ_8 (Allen et al. 2011; Vikhlinin et al. 2009). As cosmology enters the Stage-IV and Stage-V era of unprecedented survey precision, the limiting factor in extracting cosmological information from clusters is no longer statistical uncertainty but the control of systematic effects (Šarčević et al.

2025; Fumagalli et al. 2025; Gu et al. 2025, 2026). In this precision-dominated regime, accurate and internally consistent calibration of cluster mass estimates becomes essential to avoid biased cosmological inference.

The most significant of these systematics is the so-called hydrostatic mass bias. This parameter quantifies the fractional offset between the true cluster mass and the mass inferred under the assumption of hydrostatic equilibrium (HSE) applied to the hot intracluster medium (ICM), and is denoted by b_{HSE} . The HSE assumption systematically underestimates the true mass ($b_{\text{HSE}} > 0$) because it neglects non-thermal pressure support from sources such as turbulent gas motions, bulk flows, and energy injection from active galactic nuclei (Nagai et al. 2007; Nelson et al. 2014). While often modeled as a constant in cosmological analyses, its value and potential dependencies on redshift and mass remain a primary source of uncertainty.

ayodeji.ibitoye@gtiit.edu.cn

prabhakar.tiwari@gtiit.edu.cn

This uncertainty in b_{HSE} is not merely a limitation for cluster counts; it is intrinsically linked to one of the most persistent challenges to the standard ΛCDM model: the σ_8 tension. Measurements of the clustering amplitude from the primary Cosmic Microwave Background (CMB), most notably from the *Planck* satellite, favor a higher value of σ_8 (Planck Collaboration et al. 2020). In contrast, earlier low-redshift probes reported lower values (Asgari et al. 2021; Abbott et al. 2022). However, recent re-analyses, including KiDS-Legacy (Wright et al. 2025), HSC-Y3 $3\times 2\text{pt}$ (Zhang et al. 2025), and HSC-Y3 cosmic shear (Choppin de Janvry et al. 2025) yield higher S_8 values ($\sim 0.79\text{--}0.81$), reducing the historical discrepancy with *Planck* ($S_8 = 0.832$). As demonstrated by Aymerich et al. (2025) and others (Bolliet 2020; Raghunathan et al. 2022), even this evolving tension can be reconciled within ΛCDM if the b_{HSE} mass bias is significantly higher than canonical simulation calibrations, highlighting a profound degeneracy between b_{HSE} and σ_8 . Therefore, an independent, precise calibration of b_{HSE} remains imperative to determine whether the residual discrepancy signifies new physics or an unmitigated astrophysical systematics.

Past observational efforts have only achieved modest precision on b_{HSE} . Weak lensing mass calibration of *Planck* clusters yielded $\sigma(b_{\text{HSE}}) \sim 0.05\text{--}0.10$ (Planck Collaboration et al. 2016; Miyatake et al. 2019), while cross-correlation studies between *Planck* tSZ and DES weak lensing reached $\sigma(b_{\text{HSE}}) \approx 0.04$ (Pandey et al. 2022). These uncertainties are insufficient for Stage-IV/V cosmology, where sub-percent control over systematics is required to fully exploit the statistical power of next-generation data.

The path to breaking the $b_{\text{HSE}}\text{--}\sigma_8$ degeneracy lies in multi-wavelength, multi-probe observations that can directly constrain the underlying cluster gravitational potential. The power of cross-correlations to break degeneracies is now well-established in the literature. Recent work by Zhang et al. (2022) demonstrated that combining galaxy clustering and weak lensing with CMB lensing can significantly improve cosmological constraints by breaking degeneracies between parameters and systematics, particularly when moving from Stage-III to Stage-IV surveys. Their analysis focused on galaxy-CMB lensing cross-correlations ($\delta_g\kappa_{\text{CMB}}$ and $\gamma\kappa_{\text{CMB}}$). Our analysis extends this framework to the thermal Sunyaev-Zeldovich effect, where we show that tSZ-galaxy cross-correlations can obtain b_{HSE} to sub-percent precision, a critical step for resolving the σ_8 tension. Recent cosmological hydrodynamical simulations, such as FLAMINGO and The Three Hundred Project, have quantified b_{HSE} and its scatter finding a typical value of

$1 - b_{\text{HSE}} \sim 0.7\text{--}0.8$ and a complex dependence on cluster dynamical state (Braspenning et al. 2025; Corasaniti et al. 2025).

Building on these advances, forecast studies have established the potential of combining Stage-IV surveys using auto- and cross-correlations of CMB lensing, galaxy clustering, and weak lensing to suppress cosmic variance and break parameter degeneracies (Euclid Collaboration et al. 2020; Zhang et al. 2022; Ferte & Hong 2024; Xiong et al. 2025). These cross-correlations also leverage complementary redshift sensitivity: CMB lensing probes the matter distribution with a kernel peaking around $z \sim 2$ (see Figure 49 in Qu et al. (2024)), while optical weak lensing typically peaks at $z \sim 1$ (Gong et al. 2019), extending our ability to trace structure growth across cosmic time and further breaking parameter degeneracies (Zhang et al. 2022). However, many existing forecasts assume coarse or no redshift binning, leaving the critical $b_{\text{HSE}}\text{--}\sigma_8$ degeneracy largely unbroken. Our analysis demonstrates that non-tomographic analyses degrade constraints on b_{HSE} by factors of 2.5–3 compared to tomographic approaches, underscoring the essential role of fine redshift binning in achieving the sub-percent precision required for Stage-IV/V cosmology.

The next generation of surveys is poised to provide the data required for this measurement. In the optical/near-infrared, the Vera C. Rubin Observatory’s Legacy Survey of Space and Time (LSST) will deliver deep, high-resolution weak lensing shear and galaxy density maps over half the sky (LSST Science Collaboration et al. 2009). The Chinese Space Station Survey Telescope (CSST), with its unique combination of a wide field and high spatial resolution from space, will provide exceptional depth and resolution for weak lensing, complementing ground-based surveys (Gong et al. 2019, 2025; CSST Collaboration et al. 2025). In the millimeter-wave, CMB-S4 will produce a deep, high-resolution map of the CMB, enabling a nearly mass-limited catalog of clusters via the thermal Sunyaev-Zeldovich (tSZ) effect and a high-fidelity CMB lensing convergence map (Abazajian et al. 2019, 2022a). The Simons Observatory (SO), a precursor to CMB-S4, will already achieve transformative sensitivity for these measurements over a significant sky area (Hensley et al. 2022; Abitbol et al. 2025).

The unique power of our analysis lies in combining these complementary datasets. CMB-S4 and SO provide the tSZ cluster sample and CMB lensing map that is immune to the shape measurement systematics and photo- z uncertainties that affect optical weak lensing. LSST and CSST provide high-signal-to-noise galaxy density

and high-resolution weak lensing shear (γ) maps, with CSST's space-based data offering superior control of systematics on small scales. The cross-correlation between CMB lensing and optical weak lensing shear is especially powerful, as it mitigates the intrinsic alignment systematic that plagues auto-correlation analyses.

In this paper, we present a comprehensive forecast demonstrating that a joint, tomographic analysis of the cross-correlations between the tSZ effect (y), galaxy density (g), and weak lensing shear (γ), using all six associated two-point power spectra ($\mathcal{C}_\ell^{yy}, \mathcal{C}_\ell^{gg}, \mathcal{C}_\ell^{\gamma\gamma}, \mathcal{C}_\ell^{y\gamma}, \mathcal{C}_\ell^{yg}, \mathcal{C}_\ell^{\gamma g}$) can constrain b_{HSE} to sub-percent precision. We build a unified halo model pipeline and employ a Fisher matrix formalism to forecast constraints for combinations of CMB-S4, SO, LSST (Year 10), and CSST. We show that our tomographic method, using five source redshift bins, reduces the uncertainty on b_{HSE} by a factor of 2.5–3 compared to a non-tomographic analysis, directly addressing the degeneracy-breaking strategy emphasized in the CMB-S4 Science Book. This precision not only mitigates a critical systematic but also enables Stage-IV/V-level constraints on σ_8 and Ω_m , advancing a core science objective of the CMB-S4 mission. The full analysis pipeline, from survey specifications to final constraints, is summarized in Figure 3.

This paper is organized as follows: Section 2 outlines the theoretical framework, including the halo model and Limber approximation. Section 3 details the specifications of CMB-S4, Simons Observatory, LSST, and CSST. Section 4 presents the Fisher matrix formalism, power spectrum computation, and parameter space. Section 5 presents our forecasts for b_{HSE} and cosmological parameters, discusses survey-specific advantages, and summarizes implications for resolving the σ_8 tension.

Throughout, we adopt the *Planck* 2018 cosmology as our fiducial model (Planck Collaboration et al. 2020): $\Omega_m = 0.315$, $\Omega_b = 0.049$, $h = 0.674$, $\sigma_8 = 0.811$, and $n_s = 0.965$.

2. THEORETICAL FRAMEWORK

This section details the theoretical underpinnings and forecasting methodology used to quantify the constraining power of next-generation surveys on the hydrostatic mass bias and cosmological parameters. Our approach is built upon a unified halo model framework that predicts the two-point statistics of three key cosmological observables: the thermal Sunyaev–Zeldovich (tSZ) effect, galaxy number density, and weak gravitational lensing, and their tomographic cross-correlations.

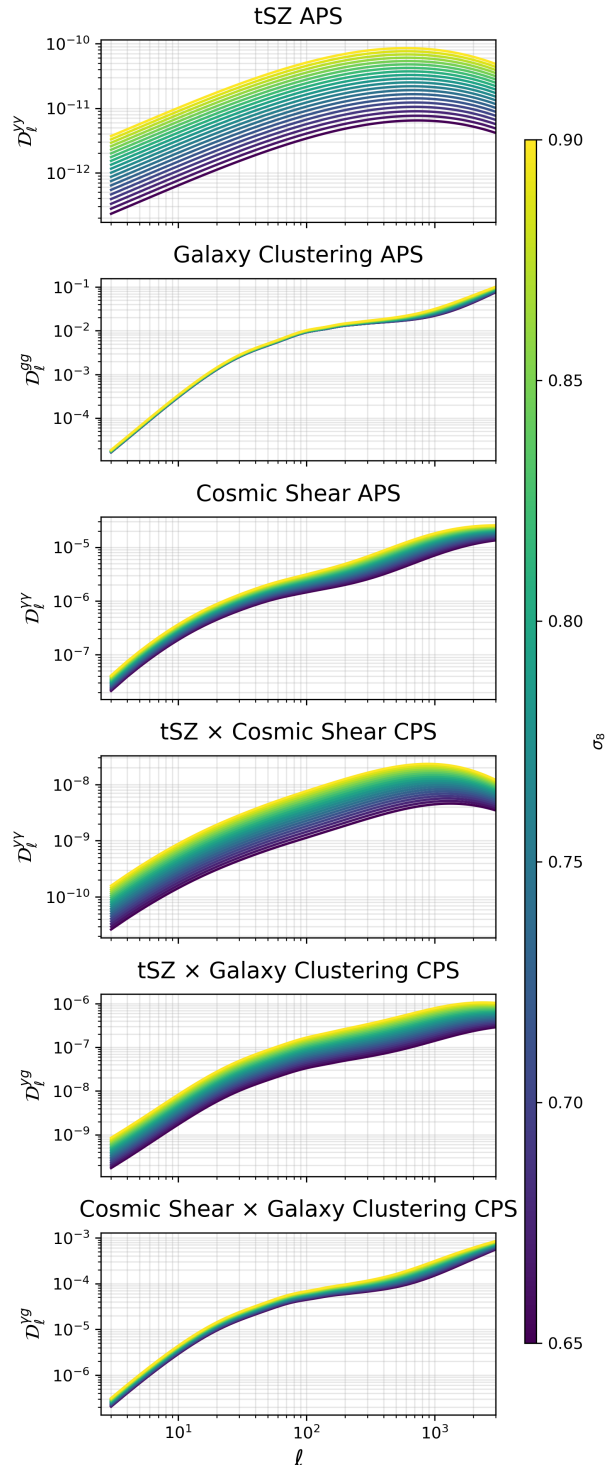


Figure 1. Stacked panels showing the sensitivity of each probe and cross-probe combination of the angular power spectra ($\mathcal{D}_\ell = \ell(\ell + 1)\mathcal{C}_\ell/(2\pi)$) for auto- and cross-correlations of the thermal Sunyaev-Zel'dovich (tSZ, y), galaxy clustering (g), and cosmic shear (γ) to the amplitude of matter density fluctuations (σ_8), with all other cosmological parameters (e.g., Ω_m, h, n_s) held fixed. APS and CPS represents angular power spectrum and cross-power spectrum, respectively.

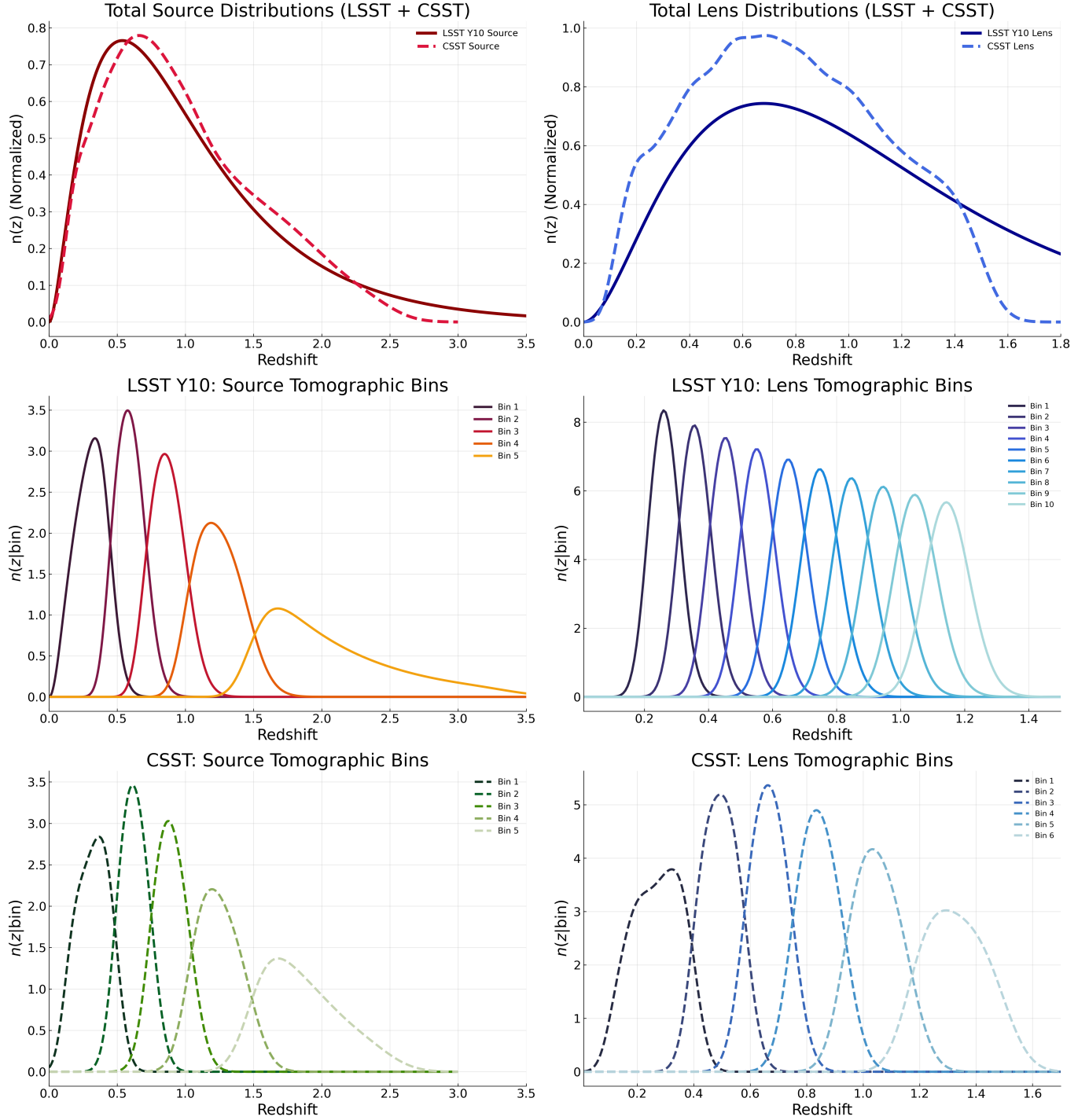


Figure 2. Normalized redshift distributions for LSST Year 10 and CSST. All distributions satisfy $\int n(z) dz = 1$, where $n(z)$ denotes the normalized redshift distribution (total: $n(z)$, tomographic bins: $n(z|\text{bin})$). Distributions include photometric redshift uncertainties convolved via the error-function formalism of [Ma et al. \(2006\)](#): $\sigma_z = 0.05(1+z)$ (LSST sources), $\sigma_z = 0.03(1+z)$ (LSST lenses), and CSST values from mission forecasts ($\sigma_z = 0.05(1+z)$ sources, $\sigma_z = 0.03(1+z)$ lenses; [Gong et al. 2019](#)). *Top row (Overplotted Totals):* Direct comparison of total distributions. Left: CSST sources extend to $z \approx 2.8$ with stronger high- z counts than LSST (spanning $z \approx 0-3.5$). Right: Both lens distributions peak at $z \approx 0.5$, with CSST extending to $z \approx 1.8$ (vs. LSST’s focus on $z \approx 0-1.5$). *Middle row (LSST Binned):* Left: 5 equal-count source bins (edges from 1% peak threshold, ensuring uniform statistical weight). Right: 10 fixed-width lens bins ($z = 0.2-1.2$, $\Delta z = 0.1$) consistent with LSST DESC conventions ([The LSST Dark Energy Science Collaboration et al. 2018](#)). *Bottom row (CSST Binned):* Left: 5 source bins optimized for tSZ-shear and cosmic shear cross-correlations. Right: 6 lens bins optimized for galaxy-tSZ and clustering cross-correlations, leveraging CSST’s superior photo- z precision. LSST distributions use parameters from the Core Cosmology Library (CCL) ([Chisari et al. 2019](#)) while CSST distributions are obtained from simulations following [Xiong et al. \(2025\)](#).

We begin with the theoretical foundation: the Halo Model (Section 2.1), which computes the three-dimensional tracer power spectra $P_{XY}(k, z)$. These 3D spectra are then projected onto the sky using the Limber Approximation (Section 2.2) to yield observable angular power spectra C_ℓ^{XY} . To reflect real-world observations, we integrate a detailed Noise Modeling component, which is combined with the signal to build a complete Covariance Matrix. The final step employs a Fisher Matrix analysis to translate this covariance into precise forecasts for parameter constraints.

2.1. Nonlinear 3D Power Spectra via the Halo Model

The halo model provides the foundational framework for describing the non-linear distribution of dark matter and its tracers across all survey combinations. It decomposes the three-dimensional power spectrum for any pair of tracers $X, Y \in \{y, g, \gamma\}$ into two physically distinct components: the 1-halo term, which governs correlations within individual halos, and the 2-halo term, which describes correlations between different halos:

$$P_{XY}(k, z) = P_{XY}^{1h}(k, z) + P_{XY}^{2h}(k, z), \quad (1)$$

where k is the comoving wavenumber (in units of h/Mpc) and z is the redshift.

2.1.1. 1-Halo and 2-Halo Contributions

The 1-halo term (P_{XY}^{1h}) dominates on small angular scales ($\ell \gtrsim 100$) and captures correlations arising from matter within individual dark matter halos. This intra-halo regime is where the hydrostatic mass bias (b_{HSE}) leaves its most pronounced imprint, as it directly modulates the inferred halo mass and its internal structure. In contrast, the 2-halo term (P_{XY}^{2h}) dominates at large scales ($\ell \lesssim 100$) and encodes correlations between distinct halos driven by linear structure growth.

Mathematically, the 1-halo and 2-halo contributions are given by (Cooray & Sheth 2002):

$$\begin{aligned} P_{XY}^{1h}(k, z) &= \int dM \frac{dn}{dM} \tilde{u}_X(k|M, z) \tilde{u}_Y(k|M, z), \quad (2) \\ P_{XY}^{2h}(k, z) &= \left[\int dM \frac{dn}{dM} b_h(M, z) \tilde{u}_X(k|M, z) \right] \\ &\quad \times \left[\int dM \frac{dn}{dM} b_h(M, z) \tilde{u}_Y(k|M, z) \right] P_{\text{lin}}(k, z), \quad (3) \end{aligned}$$

where dn/dM is the halo mass function (Tinker et al. 2008), $b_h(M, z)$ is the halo bias (Tinker et al. 2010), $\tilde{u}_X(k|M, z)$ denotes the appropriately weighted Fourier-space kernel for tracer X (including the relevant HOD or mass/pressure weighting), and $P_{\text{lin}}(k, z)$ is the linear matter power spectrum.

The modeling of these terms is tailored to each tracer. For LSST/CSST galaxy clustering, the galaxy–halo connection is described by a Halo Occupation Distribution (HOD) calibrated to the observed lens galaxy densities (n_g) and following Zheng et al. (2005). For weak lensing, the matter distribution is modeled with a Navarro–Frenk–White (NFW) density profile (Navarro et al. 1996), using the concentration–mass relation from Duffy et al. (2008) and normalized to the effective source galaxy densities (n_{eff}). For the tSZ effect, the intracluster medium pressure follows a Generalized NFW (GNFW) profile (Nagai et al. 2007; Arnaud et al. 2010), the frequency dependence of the tSZ signal is accounted for in the map and noise modeling.

The 2-halo term is proportional to the linear matter power spectrum $P_{\delta\delta}(k, z)$, computed using CAMB (Lewis et al. 2000), and scales with the large-scale bias of the tracers. The optical galaxy bias is calibrated to the survey-specific redshift distributions (dN/dz), which peak at $z \approx 0.8$ (LSST) and $z \approx 1.1$ (CSST). The tSZ bias follows ΛCDM halo bias predictions, consistent with hydrodynamical simulations (Vikhlinin et al. 2009).

The 1-halo and 2-halo terms are computed using the halo model framework implemented in the Core Cosmology Library (CCL; Chisari et al. 2019), which follows the standard formalism of Cooray & Sheth (2002). All power spectra are generated via the `halomod_Pk2D` routine, with the linear matter power spectrum $P_{\text{lin}}(k, z)$ computed using CAMB (Lewis et al. 2000). Halo properties are defined with respect to the mass $M_{200\text{m}}$, enclosed within a radius where the mean enclosed density is 200 times the mean matter density of the universe.

2.2. Angular Power Spectrum Projection

The 3D power spectra $P_{XY}(k, z)$ are projected onto the celestial sphere to yield observable angular power spectra C_ℓ^{XY} using the Limber approximation (Limber 1953), which is accurate for $\ell \gtrsim 15$:

$$C_\ell^{XY} = \int_0^{\chi_{\text{max}}} \frac{d\chi}{\chi^2} W_X(\chi) W_Y(\chi) P_{XY} \left(\frac{\ell + 1/2}{\chi}, z(\chi) \right). \quad (4)$$

Below, we specify the physical interpretation and window function $W_X(\chi)$ for each tracer.

Thermal Sunyaev–Zeldovich effect (y): The Compton- y parameter quantifies the line-of-sight integral of electron pressure in the intracluster medium (ICM), making it a nearly mass-limited tracer of collapsed halos. Unlike tracers with a fixed radial kernel, the redshift dependence of the tSZ signal is not described by a simple line-of-sight projection; instead, it is encoded through the halo-model mass and redshift integrals en-

tering the power spectrum $P_{yy}(k, z)$ and related cross-spectra. The overall tSZ amplitude is fixed to a fiducial value; our analysis varies only b_{HSE} , which rescales the inferred halo mass and thus the tSZ signal (Komatsu & Seljak 2002; Abazajian et al. 2022a).

Galaxy density (g): This tracer represents the projected overdensity of galaxies from flux-limited optical surveys such as LSST and CSST. Galaxies trace the underlying matter distribution via a linear, scale-independent bias. The corresponding window function is

$$W_g(\chi) = \frac{H(z)}{c} \frac{dN}{dz} b_g(z(\chi)), \quad (5)$$

where dN/dz is the normalized redshift distribution and $b_g(z) = 0.95(1+z)$ is our fiducial bias model, consistent with empirical measurements and Stage-IV forecasting conventions. The redshift distributions dN/dz are survey-specific and detailed in Section 3.

Weak Lensing Cosmic Shear (γ): Cosmic shear measures the coherent distortions in galaxy shapes induced by gravitational lensing from the total intervening matter distribution (dark and baryonic), making it primarily sensitive to the total matter distribution. In the Limber approximation, the shear power spectrum is equivalent to the convergence spectrum, with window function given by the lensing efficiency kernel,

$$W_\kappa(z) = \frac{3}{2} \Omega_m H_0^2 \frac{\chi(z)}{a(z)} \int_z^\infty dz \frac{dN}{dz}(z) \frac{\chi(z) - \chi(z)}{\chi(z)}, \quad (6)$$

where $a(z) = 1/(1+z)$ is the scale factor and dN/dz is the redshift distribution of the source galaxies.

The combination of galaxy clustering and weak lensing in a 3×2 pt analysis has been established as a powerful approach for Stage-IV surveys (Euclid Collaboration et al. 2020; Abazajian et al. 2019), and we extend this methodology specifically to the b_{HSE} problem.

2.2.1. Hydrostatic Mass Bias Parameterization

A central goal of this work is to constrain the hydrostatic mass bias parameter b_{HSE} , which quantifies the systematic offset between the true halo mass M and the hydrostatic mass M_{HSE} . The latter is inferred from the thermal Sunyaev–Zeldovich (tSZ) signal under the assumption of hydrostatic equilibrium in the intracluster medium (ICM) and systematically underestimates M due to unaccounted non-thermal pressure support. This relationship is defined as

$$M_{\text{HSE},\Delta} = (1 - b_{\text{HSE}})M_\Delta, \quad (7)$$

where M_Δ denotes the true halo mass enclosed within a radius R_Δ inside which the mean density is Δ times the critical density of the universe, and $M_{\text{HSE},\Delta}$ is the

mass inferred under hydrostatic equilibrium. In this work, we adopt $\Delta = 500$ (i.e., M_{500c}) for the tSZ mass–observable relation, consistent with tSZ and X-ray cluster analyses. We model b_{HSE} as a single, redshift- and mass-independent parameter with a fiducial value of $b_{\text{HSE}}^{\text{fid}} = 0.20$. This choice is consistent with recent hydrodynamical simulations (e.g., FLAMINGO and The Three Hundred Project), which find $1 - b_{\text{HSE}} \sim 0.7\text{--}0.8$ (Braspenning et al. 2025; Corasaniti et al. 2025), and aligns with the range of tSZ mass bias constraints summarized in Table 1 of Ibitoye et al. (2022).

Under the self-similar model for cluster formation, the integrated Compton- y signal scales with the true halo mass as $Y \propto M^{5/3}$. Because we assume b_{HSE} is constant, the observed tSZ signal for a given true mass is suppressed by a fixed factor of $(1 - b_{\text{HSE}})^{5/3}$. This constant scaling propagates directly into the angular power spectra: the tSZ auto-spectrum scales as $C_\ell^{yy} \propto (1 - b_{\text{HSE}})^{10/3}$, while the cross-spectra between tSZ and optical tracers scale as $C_\ell^{yg}, C_\ell^{y\gamma} \propto (1 - b_{\text{HSE}})^{5/3}$. In contrast, the auto-spectra of galaxy clustering and cosmic shear ($C_\ell^{gg}, C_\ell^{\gamma\gamma}$) remain unaffected by b_{HSE} , as they probe the total matter distribution rather than the ICM’s thermodynamic state. This differential scaling enables cross-correlations to break the degeneracy between b_{HSE} and the amplitude of matter fluctuations, σ_8 .

3. SURVEY SPECIFICATIONS AND TOMOGRAPHIC BINNING

In this section, we detail the experimental configurations, survey specifications, and tomographic binning strategies for three complementary survey combinations selected for their synergistic potential in constraining the hydrostatic mass bias (b_{HSE}) and key cosmological parameters.

3.1. Analysis Configurations

We analyze three survey combinations designed to exploit complementary strengths of next-generation CMB and optical surveys: Case A (SO \times LSST) leverages SO’s enhanced cluster mass calibration with LSST’s depth; Case B (CMB-S4 \times CSST) pairs CMB-S4’s high-fidelity tSZ mapping with CSST’s space-based optical precision; and Case C (CMB-S4 \times LSST) combines CMB-S4 with LSST’s ground-based statistical power.

These configurations exploit cross-correlations between CMB probes (tSZ) and optical probes (galaxy clustering, cosmic shear) to maximize sensitivity to b_{HSE} and break degeneracies with σ_8 . For all cases, we assume a common sky fraction $f_{\text{sky}} = 0.4$ and analyze multipoles in the range $\ell \in [30, 3000]$, capturing both linear

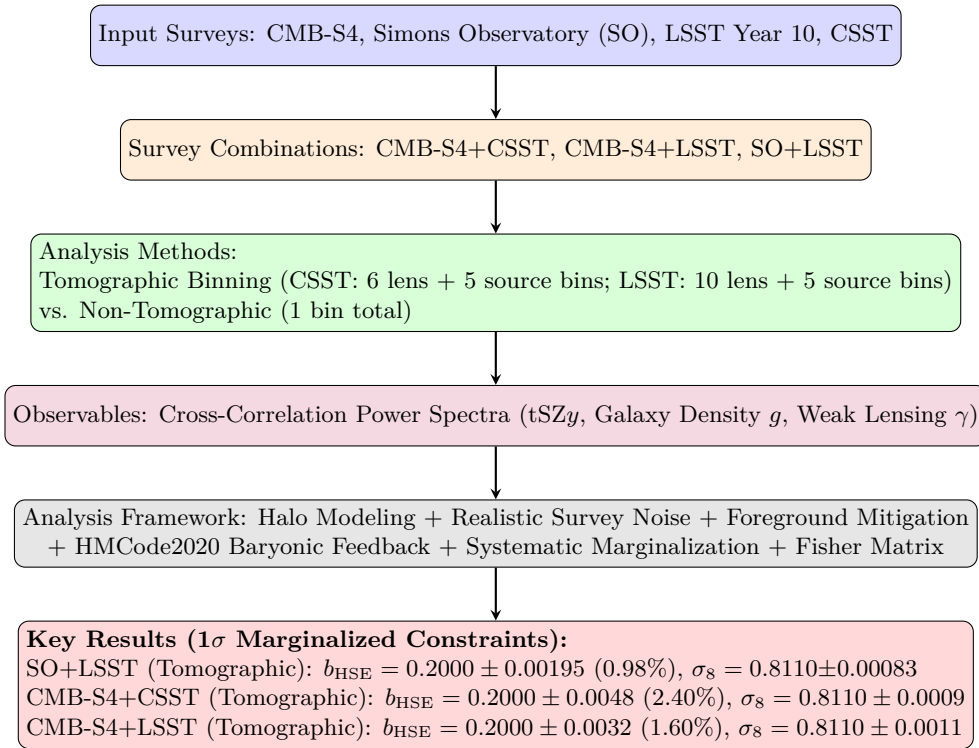


Figure 3. Analysis pipeline for forecasting hydrostatic mass bias (b_{HSE}) constraints. The workflow progresses from survey specification through tomographic/non-tomographic analysis of multi-probe power spectra to final marginalized cosmological constraints. Tomographic analyses achieve high-precision b_{HSE} constraints for SO+LSST (0.98% precision), with competitive results for CMB-S4+LSST (1.60%) and CMB-S4+CSST (2.40%).

and non-linear regimes while limiting sensitivity to the most foreground-dominated angular scales.

3.2. Survey Specifications

3.2.1. CMB Experiments

CMB-S4 is a next-generation CMB observatory, engineered to address foundational questions in cosmology via a hybrid architecture of ground-based and potential satellite assets (Gallardo et al. 2024a). For tSZ science central to constraining cluster mass-observable relations, it deploys two 6m Cross-Dragone telescopes in Chile (mapping $\sim 70\%$ of the sky daily) and a 5m Three Mirror Anastigmat telescope at the South Pole (ultra-deep 3% sky coverage) (Gallardo et al. 2024b). Operating at 95 GHz and 150 GHz (bands optimized to mitigate thermal dust foregrounds), it achieves a beam FWHM of 1.4 and polarization noise of $1 \mu\text{K-arcmin}$, with detectors cooled to 0.1 Kelvin for maximal sensitivity (Gallardo et al. 2024a,b). The experiment will field $\sim 500,000$ polarization-sensitive detectors, enabling unprecedented mapping speed for tSZ cluster detection. A key science objective includes improving constraints on cosmological parameters (e.g., σ_8) and astrophysical effects such as b_{HSE} through cross-correlations between its tSZ maps and optical probes (Gallardo et al. 2024a). Its

tSZ surveys are expected to reach lower mass threshold than SO, extending cluster detection to higher-redshift systems relevant for tracing structure growth (Abazajian et al. 2019).

The Simons Observatory (SO) serves as a critical precursor to CMB-S4, deploying a 6m Large Aperture Telescope (LAT) with 93/145 GHz bands to refine cluster cosmology methodologies (Abitbol et al. 2025). It delivers finer angular resolution (2.2 at 93 GHz, 1.4 at 145 GHz) than CMB-S4 but higher noise (8.0/10.0 $\mu\text{K-arcmin}$, respectively), trading sensitivity for early calibration power (Ade et al. 2019). SO's greatest impact for b_{HSE} studies lies in enabling early multi-probe mass calibration: when combined with optical surveys like LSST or DESI, SO's tSZ and CMB lensing maps can constrain the mean cluster mass with $\sigma(M)/M \sim 0.03$ at $z \sim 1$ (Abitbol et al. 2025), providing a benchmark for validating the mass-observable relations that CMB-S4 will rely on. Furthermore, SO's early tSZ cluster catalogs, spanning $z \lesssim 1.5$, will offer empirical constraints on the redshift evolution of b_{HSE} , reducing systematic uncertainties in CMB-S4's forecasting frameworks (Abitbol et al. 2025; Abazajian et al. 2019).

3.2.2. Optical Surveys

Table 1. Survey Specifications for Hydrostatic Mass Bias Forecasts: CMB-S4 + CSST vs. CMB-S4 + LSST vs. SO + LSST. Key results include b_{HSE} precision (tomographic/no tomographic) and tomography improvement, calculated as $[1 - (\sigma_{\text{tomo}}/\sigma_{\text{no-tomo}})] \times 100\%$. Foreground modeling uses power-law templates calibrated to post-component-separation ILC-cleaned levels. All b_{HSE} precision values reflect full marginalization over systematic uncertainties (galaxy bias perturbations, photometric redshift shifts, baryonic feedback via HMCode2020).

Parameter	CMB-S4+CSST	CMB-S4+LSST	SO+LSST
<i>CMB Specifications</i>			
Experiment	CMB-S4 Wide	CMB-S4 Wide	SO LAT
f_{sky}	0.4	0.4	0.4
Beam FWHM (145 GHz)	1.4	1.4	1.4
Temp. Noise [$\mu\text{K-arcmin}$]	1.0	1.0	1.2
ℓ Range (tSZ)	[30, 3000]	[30, 3000]	[30, 3000]
Foregrounds	CIB+radio (ILC-cleaned)	CIB+radio (ILC-cleaned)	CIB+radio (ILC-cleaned)
<i>Optical Specifications</i>			
n_{source} [arcmin^{-2}]	25.8	27	27
n_{lens} [arcmin^{-2}]	20.8	30	30
σ_{ϵ}	0.26	0.3	0.3
Source z Range	0.1–2.5	0.2–3.5	0.2–3.5
Lens z Range	0.1–1.5	0.2–1.2	0.2–1.2
$\sigma_z/(1+z)$ lenses/sources	0.03	0.05	0.05
<i>Tomography</i>			
Source Bins	5 (equal count)	5 (equal count)	5 (equal count)
Source Bin Edges	[0.10, 0.49, 0.75, 1.04, 1.48, 2.50]	[0.2, 0.5, 0.8, 1.2, 1.8, 3.5]	[0.2, 0.5, 0.8, 1.2, 1.8, 3.5]
Lens Bins	6 (optimized)	10 (fixed)	10 (fixed)
Lens Bin Edges	[0.10, 0.40, 0.58, 0.75, 0.94, 1.17, 1.50]	[0.2–1.2, 0.1 steps]	[0.2–1.2, 0.1 steps]
<i>Forecast Results</i>			
b_{HSE} Precision (Tomo)	2.40%	1.60%	0.98%
b_{HSE} Precision (No Tomo)	3.36%	5.30%	4.80%
Tomography Improvement	28.7%	69.8%	79.7%
Total Spectra	78	121	121

LSST Year 10 employs 6-band (*ugrizy*) photometry with effective source galaxy density $n_{\text{source}} = 27 \text{ arcmin}^{-2}$ (for weak lensing shear) and shape noise $\sigma_{\epsilon} = 0.3$ representative of ground-based weak lensing analyses (LSST Science Collaboration et al. 2009). For galaxy clustering (lens galaxies), we adopt $n_{\text{lens}} = 30 \text{ arcmin}^{-2}$, a subset of brighter, massive galaxies selected as large-scale structure (LSS) tracers, consistent with LSST DESC forecasting assumptions (The LSST Dark Energy Science Collaboration et al. 2018; Chang et al. 2013). The redshift distribution of the source and lens samples are modeled using Smail-type parameterizations consistent with LSST forecasting conventions; the explicit functional forms and parameters used in our analysis are specified in Section 3.3.

CSST conducts a 5-band wide-field survey with effective source galaxy density $n_{\text{source}} = 26 \text{ arcmin}^{-2}$ (for weak lensing shear) and superior shape measurement ($\sigma_{\epsilon} = 0.26$) due to space-based PSF stability (Gong

et al. 2019). For galaxy clustering, we use $n_{\text{lens}} = 25 \text{ arcmin}^{-2}$ bright, massive lens galaxies aligned with space-based survey clustering forecasts (Lin et al. 2022). Its redshift distribution is modeled with a Smail-type function extending to $z \lesssim 2.5$, consistent with mission forecasts.

For both surveys, n_{source} accounts for observational losses (blending, masking): LSST Year 10 uses $\sim 75\%$ of the raw galaxy density (reflecting 6-band photometry and optimized processing; (The LSST Dark Energy Science Collaboration et al. 2018; Chang et al. 2013)), while CSST aligns with cosmic shear simulation results for space-based surveys (Gong et al. 2019). These choices ensure consistency with our noise model (shape noise $\propto \sigma_{\epsilon}^2/n_{\text{source}}$ for shear, shot noise $\propto 1/n_{\text{lens}}$ for clustering).

3.3. Tomographic Binning

To break degeneracies between the hydrostatic mass bias b_{HSE} and cosmological parameters particularly σ_8 , we employ optimized tomographic binning schemes tailored to the redshift precision of each optical survey.

For LSST Year 10, we adopt the DESC Science Requirements Document (SRD) baseline: 10 lens bins spanning $z = 0.263\text{--}1.149$ (for galaxy clustering) and 5 source bins spanning $z = 0.309\text{--}2.053$ (for weak lensing), as shown in Figure 2. The lens bins use fixed-width redshift intervals, while the source bins are constructed to contain equal numbers of galaxies, ensuring uniform statistical weight across tomographic slices.

The underlying (true) redshift distribution follows the Smail-type form (The LSST Dark Energy Science Collaboration et al. 2018):

$$n(z) \propto \left(\frac{z}{z_0}\right)^\beta \exp\left[-\left(\frac{z}{z_0}\right)^\alpha\right]. \quad (8)$$

We adopt fiducial parameters $z_0 = 0.11$, $\alpha = 0.68$, $\beta = 2.0$ for the source sample (median redshift $z_{\text{med}} \approx 1.05$), and $z_0 = 0.28$, $\alpha = 0.90$, $\beta = 2.0$ for the lens sample. Photometric redshift uncertainties are modeled with a Gaussian scatter,

$$p(z_{\text{ph}} | z) = \frac{1}{\sqrt{2\pi} \sigma_z} \exp\left[-\frac{(z_{\text{ph}} - z)^2}{2\sigma_z^2}\right], \quad (9)$$

with $\sigma_z = 0.05(1+z)$ for sources and $\sigma_z = 0.03(1+z)$ for lenses, and with fiducial bias $z_{\text{bias}} = 0$. The resulting binned redshift distribution for the i -th tomographic bin $[z_i^{\text{min}}, z_i^{\text{max}}]$ is

$$n_i(z) = \frac{n(z)}{2} \left[\text{erf}\left(\frac{z_i^{\text{max}} - z}{\sqrt{2}\sigma_z}\right) - \text{erf}\left(\frac{z_i^{\text{min}} - z}{\sqrt{2}\sigma_z}\right) \right], \quad (10)$$

which is normalized such that $\int n_i(z) dz = 1$, following the photo- z binning formalism of Ma et al. (2006).

All distributions and binning schemes are implemented using the Core Cosmology Library (CCL) (Chisari et al. 2019), ensuring consistency with DESC forecasting standards.

For CSST, we adopt a science-driven tomographic binning scheme with 5 source bins and 6 lens bins, optimized to maximize sensitivity to the redshift-dependent cross-correlations central to our analysis: galaxy-tSZ ($\delta_g y$), tSZ-shear ($y\gamma$), and galaxy-shear ($\delta_g \gamma$). The source bins span $z \approx 0.1\text{--}2.5$, while the lens bins cover $z \approx 0.1\text{--}1.5$, with edges chosen to align with the characteristic redshift peaks of each observable (e.g., $\delta_g y$ peaks at $z \sim 0.25\text{--}0.6$).

The CSST redshift distributions are constructed from the Juitian mock galaxy light-cone simulation (Xiong et al. 2025), which models CSST’s instrumental characteristics, photometric depth, and survey strategy.

We model photometric redshift uncertainties for each individual galaxy with a Gaussian scatter, $z_{\text{obs}} \sim \mathcal{N}(z_{\text{true}}, \sigma_z)$, where $\sigma_z = \sigma_{z_0}(1+z)$. We adopt $\sigma_{z_0} = 0.05$ for the source sample and $\sigma_{z_0} = 0.03$ for the lens sample. The redshift distribution for each tomographic bin is constructed by stacking galaxies according to their redshift PDFs and normalized such that $\int n_i(z) dz = 1$. These normalized distributions are then used to compute the tracer-specific window functions for our 6×2 pt cross-correlation forecast.

This tomographic binning strategy maximizes the redshift resolution for galaxy clustering measurements while maintaining sufficient source density for weak lensing, enabling improved constraints on the hydrostatic mass bias through enhanced redshift resolution.

The refined binning strategy provides dense sampling of the redshift evolution of both the halo mass function and structure growth, which is particularly crucial for breaking the strong $b_{\text{HSE}}\text{--}\sigma_8$ degeneracy. The increased number of tomographic bins significantly enhances the cross-correlation signal between CMB and optical surveys, yielding substantial improvement in b_{HSE} constraints compared to single-bin analyses, as demonstrated in our results (see Figure 4).

We stress that, in this work, we adopt survey-optimized tomographic binning for each optical experiment, reflecting their distinct photometric precision and science goals. CSST is paired exclusively with CMB-S4, while LSST is analyzed in two configurations: (i) with CMB-S4 and (ii) with SO. The binning schemes are tailored to each combination, ensuring internal consistency within each forecast scenario.

For CMB-S4, we adopt the total temperature noise power spectrum prescribed in the CMB-S4 Science Book (2019 edition; Abazajian et al. (2019)), consistent with established modeling frameworks for ground-based CMB surveys (Abazajian et al. 2022b; Raghunathan 2022). The instrumental noise is parameterized as

$$N_\ell^{\text{CMB-S4}} = N_{\text{map}}^2 B_\ell^{-2} \left[1 + \left(\frac{\ell_{\text{knee}}}{\ell}\right)^\gamma \right], \quad (11)$$

where $N_{\text{map}} = 1.0 \mu\text{K} \cdot \text{arcmin}$ is the white-noise level per temperature map at 145 GHz. The beam transfer function is modeled as a Gaussian,

$$B_\ell = \exp\left(-\frac{\ell(\ell+1)\theta_{\text{FWHM}}^2}{8 \ln 2}\right), \quad (12)$$

with full-width-at-half-maximum $\theta_{\text{FWHM}} = 1.4'$, corresponding to CMB-S4’s large-aperture telescope. The $1/f$ noise component is characterized by a knee multipole $\ell_{\text{knee}} = 3917$ and slope $\gamma = 3.5$, following the fiducial CMB-S4 calibration (Raghunathan 2022). This

yields a white-noise floor of $N_{\ell, \text{white}} \approx 1.2 \times 10^{-7} \mu\text{K}^2$ at $\ell \gg \ell_{\text{knee}}$.

Although the tSZ auto-spectrum peaks near $\ell \sim 3000$ where white noise dominates the inclusion of the full noise model (including low- ℓ atmospheric $1/f$ noise) is essential for accurately capturing the covariance of cross-correlations involving CMB lensing and large-scale structure, which are sensitive to modes at $\ell \lesssim 100$.

In addition to instrumental noise, we include residual extragalactic foregrounds in the tSZ auto- and cross-spectra, calibrated to post-component-separation levels expected after multi-frequency internal linear combination (ILC) cleaning. Following [Camphuis et al. \(2025\)](#), we model the clustered cosmic infrared background (CIB) and radio point sources as power laws:

$$D_{\ell}^{\text{CIB}} = A_{\text{CIB}} \left(\frac{\ell}{3000} \right)^{\alpha_{\text{CIB}}}, \quad D_{\ell}^{\text{radio}} = A_{\text{radio}} \left(\frac{\ell}{3000} \right)^{\alpha_{\text{radio}}}, \quad (13)$$

where $D_{\ell} \equiv \ell(\ell+1)C_{\ell}/(2\pi)$ with amplitudes $A_{\text{CIB}} = 5.0 \times 10^{-7} \mu\text{K}^2$, $A_{\text{radio}} = 3.0 \times 10^{-7} \mu\text{K}^2$ at $\ell = 3000$, and indices $\alpha_{\text{CIB}} = -0.7$, $\alpha_{\text{radio}} = -1.2$. These correspond to residual CMB power of $C_{3000}^{\text{CIB}} \approx 3.5 \times 10^{-6} \mu\text{K}^2$ and $C_{3000}^{\text{radio}} \approx 1.4 \times 10^{-6} \mu\text{K}^2$, consistent with CMB-S4 foreground forecasts ([Abazajian et al. 2019](#)).

For the Simons Observatory (SO), we use the same noise parameterization but with SO-specific values: $\ell_{\text{knee}} = 1000$ and $\gamma = 3.5$ ([Raghunathan et al. 2022](#); [Hensley et al. 2022](#)), reflecting its distinct atmospheric noise characteristics and baseline LAT configuration. The white-noise level is set by the SO LAT map sensitivity specified in Table 1.

For galaxy clustering, shot noise in each tomographic bin is modeled as $N_{\ell}^{gg} = 1/n_g$, where n_g is the angular number density of galaxies (in steradians $^{-1}$) in that bin. Cosmic shear noise follows standard shape-noise prescriptions (see Section 3). The joint analysis assumes a sky overlap of $f_{\text{sky}} = 0.4$ between CMB and optical surveys, which is accounted for in the covariance matrix of the Fisher forecast.

All signal and noise spectra are combined to construct the full covariance matrix for the Fisher analysis (Section 4). Our modeling employs the halo framework from Section 2, with HOD for galaxies, NFW profiles for lensing, and GNFW pressure models for tSZ. We apply conservative scale cuts: $\ell < 30$ (finite sky effects), $\ell > 3000$ (baryonic uncertainties), and $\ell < 500$ for the tSZ auto-spectrum (foreground mitigation).

4. FISHER FORECAST METHODOLOGY

We employ a comprehensive Fisher matrix formalism to forecast constraints on the hydrostatic mass bias b_{HSE} and cosmological parameters from cross-correlations be-

tween CMB and optical surveys. This approach enables rigorous quantification of parameter uncertainties while accounting for all auto- and cross-correlations between tomographic bins.

4.1. Mathematical Formalism

The Fisher matrix formalism provides a powerful framework for forecasting parameter constraints from future experiments. For Gaussian-distributed observables, the data-driven Fisher matrix element (from survey power spectra and noise) for parameters θ_{α} and θ_{β} is given by:

$$F_{\alpha\beta}^{\text{data}} = \sum_{\ell=\ell_{\text{min}}}^{\ell_{\text{max}}} \frac{2\ell+1}{2} f_{\text{sky}} \text{Tr} \left(\mathbf{\Gamma}_{\ell}^{-1} \frac{\partial \mathbf{C}_{\ell}}{\partial \theta_{\alpha}} \mathbf{\Gamma}_{\ell}^{-1} \frac{\partial \mathbf{C}_{\ell}}{\partial \theta_{\beta}} \right) \quad (14)$$

where \mathbf{C}_{ℓ} is the signal covariance matrix containing all auto- and cross-power spectra between different probes and tomographic bins, $\mathbf{\Gamma}_{\ell} = \mathbf{C}_{\ell} + \mathbf{N}_{\ell}$ is the total covariance including noise \mathbf{N}_{ℓ} , f_{sky} is the sky fraction, and the factor $(2\ell+1)/2$ accounts for the number of independent modes per multipole ℓ .

To incorporate uncorrelated Gaussian priors on individual parameters (summarized in Table 3), we add the prior contribution to the diagonal of the data-driven Fisher matrix to obtain the total Fisher matrix:

$$F_{\alpha\alpha}^{\text{total}} = F_{\alpha\alpha}^{\text{data}} + \frac{1}{\sigma_{\text{prior},\alpha}^2} \quad (15)$$

The Off-diagonal elements of the total Fisher matrix remain identical to the data-driven Fisher matrix ($F_{\alpha\beta}^{\text{total}} = F_{\alpha\beta}^{\text{data}}$ for $\alpha \neq \beta$), as our priors are Gaussian and uncorrelated. No prior contribution is added for the target parameter b_{HSE} , as we impose no prior on this parameter. All other parameters include survey-specific or community-calibrated Gaussian priors (summarized in Table 3), with weak relative priors for CMB-S4 and tighter absolute priors for SO to match each survey's capabilities.

The parameter covariance matrix is obtained by inverting the total Fisher matrix:

$$\text{Cov}(\theta_{\alpha}, \theta_{\beta}) \geq [\mathbf{F}^{\text{total}, -1}]_{\alpha\beta} \quad (16)$$

with the equality holding in the limit of Gaussian likelihoods and linear parameter dependence. The 1σ uncertainty on parameter θ_{α} is then $\sigma(\theta_{\alpha}) = \sqrt{[\mathbf{F}^{\text{total}, -1}]_{\alpha\alpha}}$.

4.2. Power Spectrum Covariance and Survey Implementation

The signal covariance matrix \mathbf{C}_{ℓ} contains all auto- and cross-correlations between three primary probes:

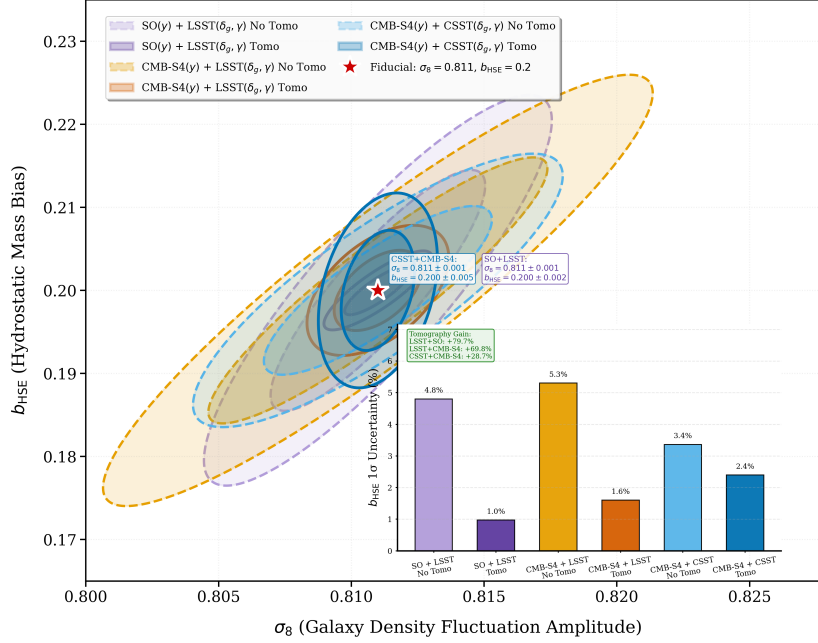


Figure 4. Constraints on hydrostatic mass bias (b_{HSE}) from Fisher matrix forecasts of CMB-optical cross-correlations, comparing CMB-S4 + CSST, CMB-S4 + LSST, and SO + LSST. **Main panel:** 68% and 95% confidence contours in the σ_8 – b_{HSE} plane. Solid/dashed curves denote tomography (CSST: 6+5 bins, LSST: 10+5 bins)/no-tomography configurations. Color coding: CMB-S4 + CSST (blue), CMB-S4 + LSST (orange), SO + LSST (purple). The black star marks the fiducial cosmology ($\sigma_8 = 0.811$, $b_{\text{HSE}} = 0.2$), consistent with the CMB-S4 Science Book’s adopted cluster mass model. **Inset:** Relative b_{HSE} precision (1 σ uncertainty as percentage of fiducial value). SO + LSST tomography achieves 0.98% precision on b_{HSE} , corresponding to sub-percent precision, and representing a 79.7% reduction in the marginalized 1 σ uncertainty relative to its no-tomography case (4.80% \rightarrow 0.98%).

thermal Sunyaev-Zel’dovich effect (y), galaxy clustering (δ_g), and cosmic shear (γ), across multiple tomographic bins. For a single tSZ map ($N_y = 1$), N_g lens bins, and N_s source bins, the total number of spectra is:

$$N_{\text{spec}} = \frac{(1 + N_g + N_s)(2 + N_g + N_s)}{2} \quad (17)$$

The covariance matrix block structure is:

$$\mathbf{C}_\ell = \begin{pmatrix} C_\ell^{yy} & C_\ell^{y\delta_g} & C_\ell^{y\gamma} \\ C_\ell^{\delta_g y} & C_\ell^{\delta_g \delta_g} & C_\ell^{\delta_g \gamma} \\ C_\ell^{\gamma y} & C_\ell^{\gamma \delta_g} & C_\ell^{\gamma \gamma} \end{pmatrix} \quad (18)$$

where each entry represents a sub-matrix spanning the relevant tomographic bin combinations. The noise covariance \mathbf{N}_ℓ includes experimental noise contributions:

$$N_\ell^{yy} = N_\ell^{\text{tSZ}} + N_\ell^{\text{fg}} \quad (\text{tSZ noise \& foregrounds}) \quad (19)$$

$$N_\ell^{\delta_g \delta_g} = \frac{1}{n_g^i} \delta_{ij} \quad (\text{shot noise per lens bin}) \quad (20)$$

$$N_\ell^{\gamma \gamma} = \frac{\sigma_s^2}{n_s^i} \delta_{ij} \quad (\text{shape noise per source bin}) \quad (21)$$

with n_g^i and n_s^i representing the galaxy density in the i -th lens bin and source bin, respectively, and cross-

correlation noise terms are neglected, assuming no correlated instrumental noise between probes. Foregrounds are modeled as a power-law combination of cosmic infrared background (CIB) and radio emission, calibrated to the residual levels expected after multi-frequency ILC cleaning ensuring their contribution to tSZ–galaxy and tSZ–shear cross-correlations is consistent with realistic survey performance.

We consider three survey combinations with specifications detailed in Table 1. The tomographic binning strategy is optimized for each survey: CMB-S4 + CSST uses 6 lens bins and 5 source bins (optimized for sensitivity to redshift-dependent cross-correlations), leveraging CSST’s superior photometric redshift precision as specified in Section 3.3; CMB-S4 + LSST employs 10 lens bins (fixed redshift intervals: $z \in [0.2, 1.2]$) and 5 source bins (equal counts), utilizing LSST’s high source density and wide redshift coverage; and SO + LSST uses identical tomographic binning to CMB-S4 + LSST, enabling direct comparison of CMB experiment capabilities. The multipole range $\ell \in [30, 3000]$ captures the relevant scales for cluster and large-scale structure science, while limiting sensitivity to very small scales where baryonic effects and non-linear modeling uncertainties become significant.

4.3. Parameter Space and Halo Model Framework

Our Fisher analysis employs a comprehensive parameter space that fully marginalizes over key systematic uncertainties:

$$\theta = \underbrace{\{\Omega_m, \Omega_b, \sigma_8, h, n_s\}}_{\Lambda\text{CDM}} \cup \underbrace{\{b_{\text{HSE}}, \log_{10}(T_{\text{AGN}}/\text{K}), A_{\text{IA}}, \eta_{\text{IA}}\}}_{\text{Astrophysics}} \cup \underbrace{\{b_{g,i}, \Delta z_{\text{lens},i}, \Delta z_{\text{src},j}\}}_{\text{Nuisance}} \quad (22)$$

The hydrostatic mass bias b_{HSE} enters the tSZ power spectra through the mass-pressure relation:

$$C_\ell^{yy} \propto (1 - b_{\text{HSE}})^{10/3}, \quad C_\ell^{y\delta_g} \propto (1 - b_{\text{HSE}})^{5/3}, \quad (23)$$

reflecting its impact on both tSZ auto-correlation and cross-correlation with galaxies.

Baryonic feedback is modeled via HMCODE2020 with $\log_{10}(T_{\text{AGN}}/\text{K})$ as a free parameter (fiducial 7.8, prior $\sigma = 0.3$), calibrated to BAHAMAS hydrodynamical simulations. Intrinsic alignments use the NLA model with redshift evolution parameter η_{IA} (fiducial 0, prior $\sigma = 0.5$), per DESC SRD (2024). Nuisance parameters include:

Galaxy bias perturbations $b_{g,i} = b_g^{\text{fid}}(z) \times (1 + \delta b_{g,i})$ for each lens bin ($i = 1, \dots, 10$ for LSST; $i = 1, \dots, 6$ for CSST), with Gaussian priors $\sigma(\delta b_{g,i}) = 0.05$, photo- z mean shift parameters $\Delta z_{\text{lens},i}$ and $\Delta z_{\text{src},j}$ for all tomographic bins, with DESC SRD priors $\sigma(\Delta z_{\text{lens}}) = 0.002(1+z)$ and $\sigma(\Delta z_{\text{src}}) = 0.005(1+z)$.

All power spectra are computed using the halo model framework in CCL. We employ the [Tinker et al. \(2008\)](#) halo mass function (200m definition) and [Tinker et al. \(2010\)](#) halo bias. Galaxy clustering uses an HOD model with fiducial bias $b_g^{\text{fid}}(z) = 0.95(1+z)$, weak lensing uses NFW profiles with [Duffy et al. \(2008\)](#) concentration, and tSZ uses generalized NFW pressure profiles with [Arnaud et al. \(2010\)](#) parameters.

We adopt a Planck 2018 ΛCDM cosmology as fiducial: $\{\Omega_m = 0.315, \sigma_8 = 0.811, h = 0.674, n_s = 0.9649, \Omega_b = 0.0486\}$, with $b_{\text{HSE}} = 0.2$. The Fisher matrix is computed via central finite differences ($\Delta\theta_\alpha = 0.01\theta_\alpha$), with covariance including survey noise, foregrounds, and tomographic binning via block matrix assembly. No prior is imposed on b_{HSE} .

4.4. Probe Decomposition Analysis

To quantify the synergy between multi-probe observables, we perform a probe decomposition analysis for all survey combinations, isolating contributions from tSZ auto-correlations (C_ℓ^{yy}), tSZ-galaxy cross-correlations (C_ℓ^{gy}), and galaxy clustering (C_ℓ^{gg}). For all tomographic

configurations, the joint $yy + gy + gg$ combination delivers the tightest constraints on b_{HSE} , with gy cross-correlations playing a key role in mitigating degeneracies between b_{HSE} and σ_8 .

A tSZ auto-spectrum-only analysis (with Planck priors) yields $\sigma(b_{\text{HSE}}) = 0.0255$ (12.8%), demonstrating that cross-correlations with LSST large-scale structure are essential to achieve percent-level calibration, even when external CMB information is available. Optical-only probes, including galaxy clustering (gg), cosmic shear ($\gamma\gamma$), and their combination in the standard 3×2 pt analysis (i.e., $gg + \gamma\gamma + g\gamma$), provide no significant constraint on b_{HSE} , as they lack direct sensitivity to the thermal pressure field. By contrast, these same optical probes deliver strong constraints on σ_8 : 3×2 pt alone achieves $\sigma(\sigma_8) = 0.00106$ (0.13%), comparable to CMB-only forecasts. The inclusion of tSZ cross-correlations further refines this to $\sigma(\sigma_8) = 0.00083$ (0.10%) in the full combination, while simultaneously enabling the first sub-percent constraint on b_{HSE} .

Although the tSZ auto-spectrum exhibits the largest absolute response to changes in σ_8 (see top panel of [Figure 1](#)), its constraining power on σ_8 is limited by cosmic variance and residual foregrounds even with SO's ultra-low instrumental noise ($1.2 \mu\text{K-arcmin}$). In contrast, galaxy clustering (gg) and 3×2 pt achieve tighter σ_8 constraints due to superior signal-to-noise at low multipoles, where σ_8 is most sensitively probed. This illustrates that final parameter precision depends on the interplay of sensitivity, noise, and cosmic variance rather than sensitivity alone. The gy cross-correlations resolve the b_{HSE} limitation by linking the tSZ signal (a direct mass tracer) to galaxy overdensities (a large-scale structure tracer). For SO + LSST tomography, gy contributes more than 60% of the Fisher information for b_{HSE} , yielding $\sigma(b_{\text{HSE}}) = 0.00195$ (0.98%) in the full combination. Tomography amplifies this synergy by reducing redshift-dependent degeneracies across multiple bins.

4.5. Systematics and Prior Choices

We marginalize over all dominant astrophysical and observational systematics relevant to Stage-IV CMB and optical surveys, with priors calibrated to community standards ([The LSST Dark Energy Science Collaboration et al. 2018](#)) and validated by DES Y1 results ([To et al. 2021](#)). Baryonic feedback is modeled via HMCODE2020 ([Mead et al. 2021](#)), parameterized by $\log_{10}(T_{\text{AGN}}/\text{K})$ (fiducial = 7.8, Gaussian prior $\sigma = 0.3$ from BAHAMAS simulations). The GNFW pressure profile parameters (P_0, c_{500}) are fixed to X-ray-calibrated universal values ([Arnaud et al. 2010](#)), as our forecasts show no significant improvement on

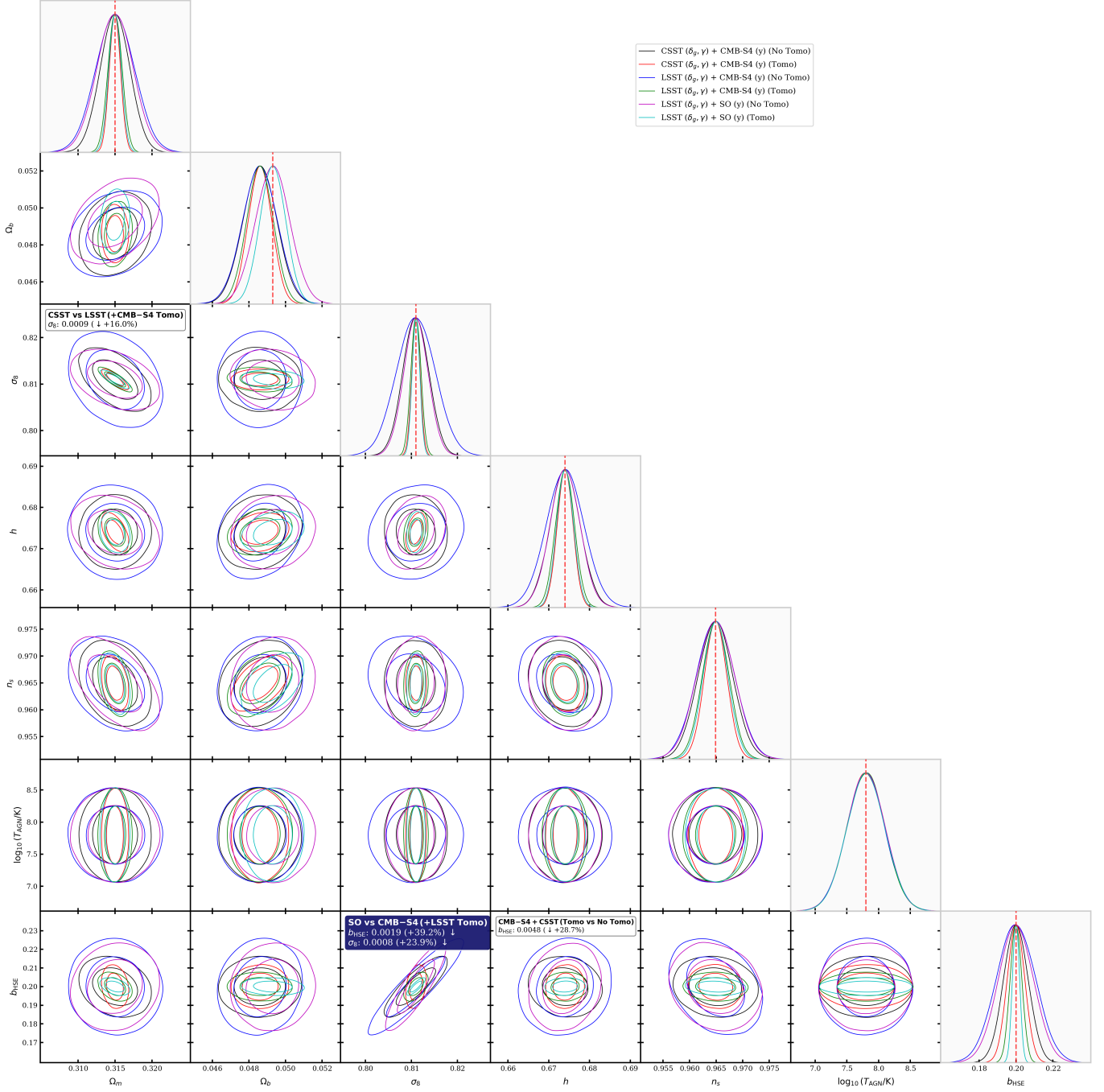


Figure 5. Multi-parameter constraints from cross-correlation analyses combining CMB and optical surveys. The corner plot shows 1σ and 2σ confidence contours for five selected cosmological and astrophysical parameters: the matter fluctuation amplitude σ_8 , hydrostatic mass bias b_{HSE} , matter density Ω_m , Hubble constant h , and intrinsic alignment amplitude A_{1A} . Four survey configurations are compared: CMB-S4 + CSST without tomography (blue dashed), CMB-S4 + CSST with tomography (blue solid), CMB-S4 + LSST with tomography (orange solid), and SO + LSST with tomography (purple solid). The significant tightening of constraints with tomography demonstrates the power of redshift binning in breaking parameter degeneracies, particularly for b_{HSE} which shows precision improvements from 29% (CMB-S4+CSST) to 79.7% (SO+LSST) with tomographic analyses.

the $\log_{10}(T_{\text{AGN}}/\text{K})$ prior across all survey combinations. TSZ cross-correlations probe ICM thermal pressure, whose uncertainty is absorbed by b_{HSE} and GNFW parameters rather than matter clustering amplitude, which aligns with (The LSST Dark Energy Science Collaboration et al. 2018) that found weak baryonic constraints from cosmic shear alone. While hydrodynamical simulations indicate correlated suppression of small-scale clustering and Compton- y signal under stronger AGN feedback (Battaglia et al. 2012; Le Brun et al. 2015; Harnois-Déraps et al. 2015; McCarthy et al. 2017), a self-consistent joint model linking matter and pressure profiles remains an open challenge, so we adopt independent modeling following current multi-probe practice Mead et al. (2021); The LSST Dark Energy Science Collaboration et al. (2018). For intrinsic alignments, we use the NLA model with two parameters: amplitude A_{IA} and redshift evolution η_{IA} , applying Gaussian priors $\sigma(A_{\text{IA}}) = 0.50$ and $\sigma(\eta_{\text{IA}}) = 0.50$ (both surveys) consistent with DESC SRD recommendations but simplified by omitting luminosity and high-redshift scaling terms, a standard approach for baseline forecasts. For observational systematics, we include per-tomographic-bin galaxy bias perturbations ($\delta b_{g,i}$) and photometric redshift shifts ($\Delta z_{\text{lens}}, \Delta z_{\text{src}}$) with conservative Gaussian priors: $\sigma(\delta b_{g,i}) = 0.05$, $\sigma(\Delta z_{\text{lens}}) = 0.002(1+z)$, and $\sigma(\Delta z_{\text{src}}) = 0.005(1+z)$, which matches the SRD’s Y10 Cluster requirement CL2. Fiducial values (e.g., $b_{\text{HSE}} = 0.2$, $\sigma_8 = 0.811$) follow Planck 2018 ΛCDM (Aghanim et al. 2020) cluster mass calibration studies. Marginalized constraints on nuisance parameters are shown in Appendix A.2. Secondary systematics (e.g., cluster misalignments, pressure profile deviations, CMB beam and optical shear calibration errors) are subdominant for Stage-IV performance and expected to contribute $< 0.5\%$ additional uncertainty to b_{HSE} . All priors are intentionally wide to ensure constraints are driven by data, not assumptions, consistent with The LSST Dark Energy Science Collaboration et al. (2018) and To et al. (2021).

4.6. Robustness Tests

To ensure our constraints are not driven by optimistic assumptions, we perform five robustness checks on our fiducial SO + LSST tomographic forecast (Section 5.1). First, varying the maximum multipole from the baseline $\ell_{\text{max}} = 3000$ to $\ell_{\text{max}} = 2000$ or 1500 degrades $\sigma(b_{\text{HSE}})$ from 0.98% to 1.48% (+51%) and 2.00% (+104%), respectively. This degradation occurs because the tSZ power spectrum peaks at $\ell \sim 2000\text{--}3000$, where most of the Fisher information on b_{HSE} resides. The high-precision calibration of hydrostatic bias thus relies crit-

ically on nonlinear, small-scale modes precisely those accessible to SO’s low-noise, high-resolution measurements.

Second, widening or tightening the $\log_{10}(T_{\text{AGN}}/\text{K})$ prior by a factor of two changes $\sigma(b_{\text{HSE}})$ by only $\sim 0\%$ (since $\log_{10}(T_{\text{AGN}})$ is unconstrained), indicating minimal sensitivity to baryonic feedback modeling. Third, doubling or halving the photometric redshift shift priors ($\Delta z_{\text{lens}}, \Delta z_{\text{src}}$) alters $\sigma(b_{\text{HSE}})$ by +2% to -4% , identifying photo- z calibration as a negligible systematic for b_{HSE} . Fourth, removing all external Planck CMB priors on ΛCDM parameters degrades $\sigma(b_{\text{HSE}})$ from 0.98% to 1.00% (+2%). Crucially, the constraint remains at the sub-percent level, demonstrating that tSZ–optical cross-correlations not external CMB information provide the foundational calibration of hydrostatic mass bias. Planck priors offer negligible refinement for b_{HSE} . Finally, alternative nuisance parameter specifications (e.g., $\sigma(\Delta z_{\text{src}}) = 0.003$ vs. 0.005) yield consistent results, confirming prior robustness. Together, these tests confirm that our sub-percent b_{HSE} constraint is data-driven, stable, and anchored in the multi-probe synergy of SO and LSST.

5. RESULTS & SUMMARY

Our Fisher forecast analysis demonstrates that tomographic cross-correlations between next-generation CMB (CMB-S4, Simons Observatory/SO) and optical (LSST, CSST) surveys will deliver improved constraints on the hydrostatic mass bias parameter b_{HSE} and core cosmological parameters. These results are derived from a halo model framework incorporating realistic noise, foregrounds, and photometric redshift uncertainties (Abazajian et al. 2019; The LSST Dark Energy Science Collaboration et al. 2018; Xiong et al. 2025; Abitbol et al. 2025).

5.1. Hydrostatic Mass Bias Constraints

The most striking finding is the substantial improvement in b_{HSE} precision enabled by tomography, though the magnitude of gain varies across survey combinations (Table 1). Our forecasts yield 1σ constraints on b_{HSE} (fiducial = 0.20) with the tightest constraint achieved by SO + LSST tomography at 0.98%, down to 5.30% for CMB-S4 + LSST without tomography.

Tomography drives precision gains of 28.6% for CMB-S4 + CSST (3.36% \rightarrow 2.40%), 69.8% for CMB-S4 + LSST (5.30% \rightarrow 1.60%), and 79.7% for SO + LSST (4.80% \rightarrow 0.98%). The higher galaxy density of LSST (27 arcmin $^{-2}$ vs. CSST’s 22 arcmin $^{-2}$) and its 10 lens/5 source bins amplify tomography gains, while SO’s ultra-low tSZ noise (1.2 μK -arcmin at 145 GHz) enables sub-

percent mass calibration when combined with LSST tomography.

Notably, the SO + LSST tomographic constraint ($\sigma(b_{\text{HSE}}) = 0.00195$) achieves 0.98% precision, sufficient to meet the CMB-S4 Science Book’s requirement for sub-percent cluster mass calibration and help resolve the σ_8 tension between CMB and large-scale structure probes (Planck Collaboration et al. 2020). This surpasses even optimistic projections for current cluster surveys, marking a leap from b_{HSE} as a limiting systematic to a precision-constrained parameter. Given SO’s ongoing operations and competitive performance, our results establish SO + LSST as the leading near-term pathway to sub-percent hydrostatic mass bias calibration via tSZ cross-correlations.

5.2. Cosmological Parameter Constraints

The sensitivity of individual probes and their cross-correlations to σ_8 is illustrated in Figure 1, which shows that tSZ–shear and galaxy–tSZ cross-spectra provide complementary leverage across multipoles. All tomographic configurations achieve Stage-IV/V-level constraints on core cosmological parameters (Table 2). When marginalizing over b_{HSE} , baryonic feedback $\log_{10}(T_{\text{AGN}}/\text{K})$, and intrinsic alignments ($A_{\text{IA}}, \eta_{\text{IA}}$), we find: SO + LSST delivers the tightest constraints with $\sigma(\sigma_8) = 0.00083$ (0.10%), $\sigma(\Omega_m) = 0.00083$ (0.26%), and $\sigma(h) = 0.00204$ (0.30%); CMB-S4 + CSST achieves $\sigma(\sigma_8) = 0.00092$, $\sigma(\Omega_m) = 0.00075$, $\sigma(h) = 0.00193$; and CMB-S4 + LSST yields $\sigma(\sigma_8) = 0.00109$, $\sigma(\Omega_m) = 0.00095$, $\sigma(h) = 0.00231$. These results are competitive with standalone CMB or optical surveys, but with the added robustness of multi-probe synergy and full systematic marginalization.

Intrinsic alignment ($A_{\text{IA}}, \eta_{\text{IA}}$) is tightly controlled in tomographic setups, with marginalized uncertainties reduced by factors of 3–5 compared to non-tomographic analyses. This highlights tomography’s unique ability to isolate lensing signals from redshift-dependent systematics, a critical advantage for weak lensing cosmology that also strengthens constraints on cluster-based cosmological probes like the tSZ effect.

5.3. Degeneracy Breaking, Parameter Correlations

The multi-parameter corner plot (Figure 5) reveals critical degeneracy patterns, with tomography playing a pivotal role in breaking the fundamental $b_{\text{HSE}}-\sigma_8$ correlation. For SO + LSST, tomographic cross-correlations reduce the 2D contour area for this pair by $\sim 80\%$ compared to non-tomographic analyses, enabling simultaneous precision constraints on both parameters.

A defining feature of our constraints is the evolution of key parameter degeneracies, driven by tomographic

Table 2. Forecasted 1σ constraints on key cosmological parameters from *tomographic* multi-probe analyses, fully marginalized over b_{HSE} (fiducial = 0.20), $\log_{10}(T_{\text{AGN}}/\text{K})$, intrinsic alignment parameters ($A_{\text{IA}}, \eta_{\text{IA}}$), galaxy bias perturbations, and photometric redshift shifts. All uncertainty values are reported in units of 10^{-3} .

<i>Tomographic Survey Combinations</i>			
Survey Combination	$\sigma(\sigma_8) \times 10^3$	$\sigma(\Omega_m) \times 10^3$	$\sigma(h) \times 10^3$
SO + LSST	0.83	0.80	2.04
CMB-S4 + CSST	0.92	0.75	1.93
CMB-S4 + LSST	1.09	0.95	2.31

information and synergy between probes. In the $\Omega_m-\sigma_8$ plane, no-tomography analyses produce tight, negatively sloped anticorrelations a signature of averaging signals across redshifts. Tomography tightens this degeneracy via redshift-resolved distance information, preserving its anticorrelated direction for CMB-S4+CSST/LSST. Notably, the SO+LSST no-tomography case weakens this anticorrelation: SO’s tSZ signal (sensitive to total cluster abundance) introduces a competing positive correlation between Ω_m and σ_8 , partially canceling the negative clustering anticorrelation. This competition vanishes in SO+LSST tomography, where LSST’s redshift-resolved data dominates, restoring the standard $\Omega_m-\sigma_8$ anticorrelation while significantly improving precision.

The $b_{\text{HSE}}-\sigma_8$ plane exhibits an even more striking degeneracy breakdown. In no-tomography cases, b_{HSE} and σ_8 are nearly indistinguishable their effects on the observed signal are conflated when averaging across redshifts. Tomography resolves this ambiguity by leveraging redshift-dependent b_{HSE} behavior: hydrostatic mass bias varies with cluster mass (and thus redshift), while σ_8 is redshift-independent. By comparing signals across tomographic bins, we separate the redshift-varying apparent amplitude (from b_{HSE}) from the redshift-constant intrinsic amplitude (from σ_8), thereby substantially reducing the degeneracy.

The $b_{\text{HSE}}-\Omega_m$ degeneracy exhibits survey-specific behavior: most combinations show moderate anti-correlation, while SO + LSST significantly weakens this anti-correlation. This unique performance stems from SO’s ultra-low tSZ noise and LSST’s high-density tomography, which provide independent constraints on Ω_m (via galaxy clustering) and b_{HSE} (via redshift-dependent tSZ–shear cross-correlations).

Notably, non-tomographic configurations show contrasting $A_{\text{IA}}-\Omega_m$ correlations: CMB-S4 + LSST (No Tomo) exhibits anti-correlation, while CMB-S4 + CSST

(No Tomo) shows weak correlation. These differences arise from survey-specific properties. LSST’s wider redshift coverage and CSST’s tighter photometric redshift precision, which cause non-tomographic analyses to partially conflate intrinsic alignments (redshift-dependent) with cosmological structure growth. Tomography eliminates this ambiguity, with all tomographic setups showing minimal A_{IA} –cosmology correlations, indicating self-calibration of intrinsic alignments without degrading constraints.

These results underscore two critical insights: (1) probe synergy (e.g., SO+LSST) can modify degeneracies even without tomography, and (2) tomography’s unique power lies in prioritizing redshift-dependent information disentangling systematic effects (like b_{HSE}) from cosmological parameters (like Ω_m and σ_8), reasserting physical parameter relations, and maximizing precision for precision cosmology.

The total information content quantified by the number of independent power spectra, ranges from 78 (CSST tomography: 6 lens \times 5 source + tSZ-auto + cross terms) to 121 (LSST tomography: 10 lens \times 5 source + tSZ terms), reflecting the leverage of tomographic binning in breaking degeneracies.

5.4. Survey-Specific Advantages and Cosmological Implications

Each combination demonstrates distinct strengths with profound implications for cluster cosmology. For instance, the CMB-S4 + CSST benefits from CSST’s space-based advantages (superior image quality, tighter photo- z uncertainties: $\sigma_z/(1+z) = 0.03$) to deliver competitive b_{HSE} precision (2.40% tomographic) with modest tomography gains (28.7%), positioning it as a cost-effective complement to ground-based surveys. Although CMB-S4 + LSST uses LSST’s high galaxy density and wide redshift coverage to achieve 1.60% b_{HSE} precision, with 69.8% tomography improvement, it excels in balancing cluster bias and cosmological constraints. However, SO + LSST: SO’s ultra-low tSZ noise (1.2 μ K-arcmin at 145 GHz) and optimized frequency coverage combine with LSST’s deep tomography to set the gold standard, with 0.98% b_{HSE} precision. Even without tomography, SO + LSST achieves a competitive 4.80% constraint on b_{HSE} comparable to the non-tomographic performance of CMB-S4 + LSST (5.30%)

and already sufficient for Stage-IV science. When combined with tomography, SO + LSST reaches 0.98%, surpassing even CMB-S4-based configurations.

These results mark a paradigm shift: high-precision b_{HSE} constraints (0.98–2.40% for tomographic configurations) will reduce cluster mass calibration uncertainties from a dominant systematic to a sub-dominant one, enabling σ_8 measurements from cluster abundances with sub-percent statistical uncertainty after marginalizing over key systematics. Tomographic cross-correlations provide a self-calibration pathway for b_{HSE} independent of X-ray or SZ scaling relations, mitigating circularity in mass calibration.

For the σ_8 tension, SO + LSST’s 0.98% b_{HSE} precision and 0.00083 $\sigma(\sigma_8)$ will enable discrimination between competing explanations (e.g., new physics vs. systematic mismodeling). Meanwhile, CSST and LSST’s complementary coverage offers cross-validation, ensuring robustness of results.

In summary, tomographic cross-correlations between CMB and optical surveys will transform cluster cosmology. SO + LSST tomography leads with 0.98% b_{HSE} precision, CMB-S4 + LSST balances sensitivity and accessibility, and CMB-S4 + CSST provides a viable alternative with space-based advantages. The varying but substantial tomography gains (28.7–79.7%) underscore redshift binning as a foundational tool for breaking degeneracies, paving the way for a new era of precision in structure formation and cosmological parameter inference.

ACKNOWLEDGMENTS

We thank the CMB-S4, Simons Observatory, LSST/DESC, and CSST collaborations for making public their science requirements, redshift distributions, and instrumental specifications. This work was supported by Guangdong Technion startup funds. YG acknowledges the support from National Key R&D Program of China grant Nos. 2022YFF0503404 and 2020SKA0110402, the CAS Project for Young Scientists in Basic Research (No. YSBR-092), and science research grants from the China Manned Space Project with grant Nos. CMS-CSST- 2025-A02. All results presented here are theoretical forecasts based on published survey specifications; no observational data were used.

APPENDIX

Table 3. Prior specifications for Fisher forecast parameters (CMB-S4 + LSST/CSST surveys). All priors are absolute unless noted as relative (scaled to fiducial value or redshift). References: HMCode2020 (Mead et al. 2021), DESC SRD 2018 (The LSST Dark Energy Science Collaboration et al. 2018), DES Y1 (To et al. 2021), Planck 2018 (Aghanim et al. 2020).

Parameter	Fiducial	Prior σ (Baseline / Tested)	Source/Justification
<i>ΛCDM Cosmology (Aghanim et al. 2020)</i>			
Ω_m	0.315	0.007 (abs; SO) / 1% rel (CMB-S4)	Planck 2018 / CMB-S4 Sci. Book
Ω_b	0.0493	0.001 (abs) / —	Planck 2018 / BBN
σ_8	0.811	0.006 (abs; SO) / 1% rel (CMB-S4)	Planck 2018 / CMB-S4 Sci. Book
h	0.674	1% rel (CMB-S4) / 0.01 (abs; SO)	Planck 2018 / CMB-S4 Sci. Book
n_s	0.9649	0.004 (abs) / —	Planck 2018
<i>Astrophysical Systematics</i>			
b_{HSE}	0.2	None (target) / —	CMB cluster cal. / HMCode2020
$\log_{10}(T_{\text{AGN}}/\text{K})$	7.8	0.3 (abs) / 0.15, 0.60	HMCode2020 / BAHAMAS sims
A_{IA}	1.0	10% rel (0.10) / 0.50 (abs)	NLA model (DES Y1 / DESC SRD)
η_{IA}	0.0	0.50 (abs) / —	NLA model (DES Y1 / DESC SRD)
<i>Nuisance Parameters (per tomographic bin)</i>			
$\delta b_g^{(i)}$	0.0	0.05 (abs) / —	DESC SRD 2018
$\Delta z_{\text{lens}}^{(i)}$	0.0	0.002(1+z) / 0.001, 0.004	DESC SRD 2018 (LSS1 Y10)
$\Delta z_{\text{src}}^{(j)}$	0.0	0.003(1+z) / 0.005, 0.010	DESC SRD 2018 (WL1 Y10)

A. SUPPLEMENTARY METHODOLOGICAL DETAILS

A.1. Prior Specifications for Fisher Forecast Parameters

Full prior specifications for all parameters in our Fisher forecast analysis are provided in Table 3. The methodology and physical motivation for these choices are detailed in Section 4.5.

A.2. Galaxy Bias and Photometric Redshift Uncertainty Models

Figures 6 and 7 show marginalized 1σ constraints on tomographic nuisance parameters for the three survey combinations: SO+LSST (baseline), CMB-S4+LSST, and CMB-S4+CSST. Violin plots represent the full uncertainty distribution per redshift bin, with white markers indicating the mean constraint.

For galaxy bias perturbations ($\delta b_g^{(i)}$), SO+LSST achieves the tightest average constraint ($\langle\sigma(\delta b_g)\rangle = 0.00128$), outperforming CMB-S4+LSST (0.00150, -16.5%) and CMB-S4+CSST (0.00134, -4.6%). For photometric redshift shifts, SO+LSST also sets the benchmark: lens photo- z shifts are constrained to $\langle\sigma(\Delta z_{\text{lens}})\rangle = 0.00038$, while source photo- z shifts reach $\langle\sigma(\Delta z_{\text{src}})\rangle = 0.00191$. All results reflect full marginalization over cosmological and astrophysical parameters, demonstrating the robustness of our systematics modeling.

REFERENCES

- Abazajian, K., Addison, G., Adshead, P., et al. 2019, arXiv e-prints, arXiv:1907.04473, doi: [10.48550/arXiv.1907.04473](https://doi.org/10.48550/arXiv.1907.04473)
- Abazajian, K., Abdulghafour, A., Addison, G. E., et al. 2022a, arXiv e-prints, arXiv:2203.08024, doi: [10.48550/arXiv.2203.08024](https://doi.org/10.48550/arXiv.2203.08024)
- Abazajian, K., Addison, G. E., Adshead, P., et al. 2022b, ApJ, 926, 54, doi: [10.3847/1538-4357/ac1596](https://doi.org/10.3847/1538-4357/ac1596)
- Abbott, T. M. C., Aguena, M., Alarcon, A., et al. 2022, PhRvD, 105, 023520, doi: [10.1103/PhysRevD.105.023520](https://doi.org/10.1103/PhysRevD.105.023520)
- Abitbol, M., Abril-Cabezas, I., Adachi, S., et al. 2025, JCAP, 2025, 034, doi: [10.1088/1475-7516/2025/08/034](https://doi.org/10.1088/1475-7516/2025/08/034)
- Ade, P., Aguirre, J., Ahmed, Z., et al. 2019, JCAP, 2019, 056, doi: [10.1088/1475-7516/2019/02/056](https://doi.org/10.1088/1475-7516/2019/02/056)
- Aghanim, N., et al. 2020, Astron. Astrophys., 641, A6, doi: [10.1051/0004-6361/201833910](https://doi.org/10.1051/0004-6361/201833910)

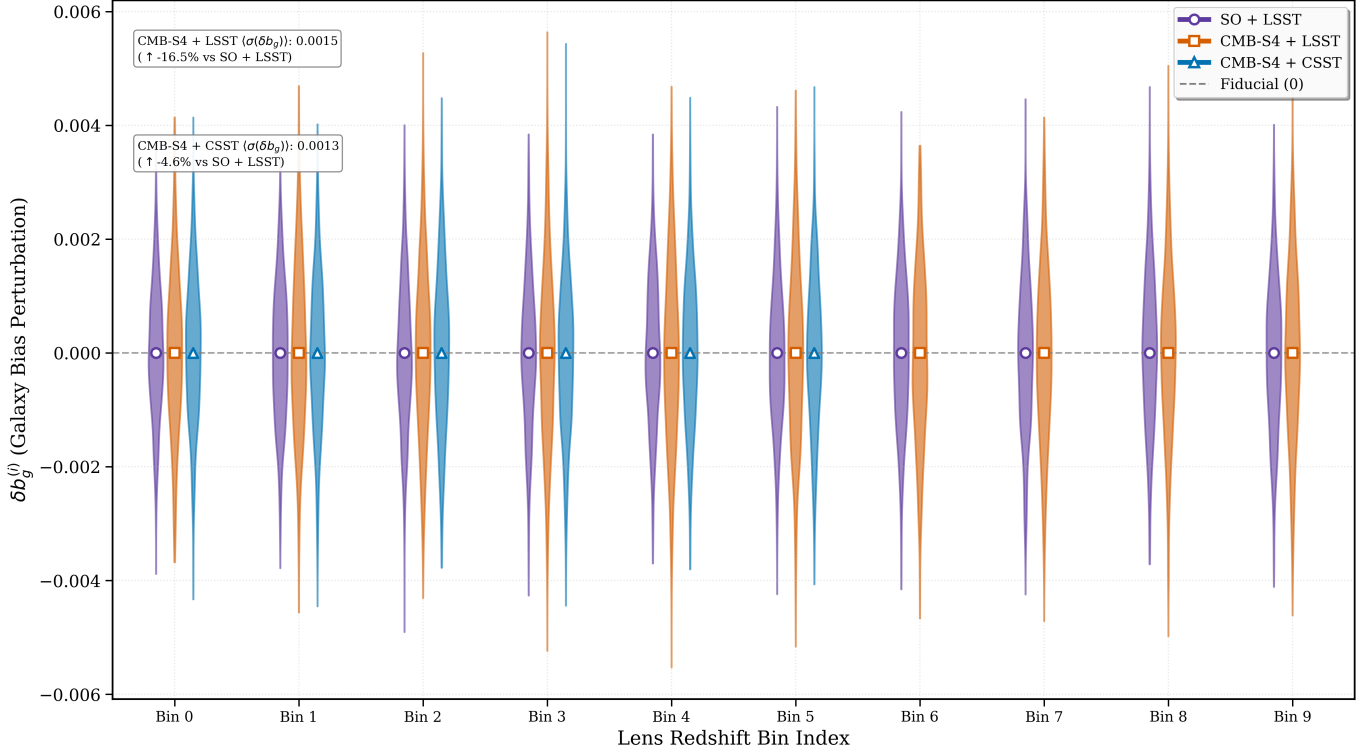


Figure 6. Constraints on galaxy bias perturbation nuisance parameters $\delta b_g^{(i)}$ for tomographic survey combinations: SO+LSST (purple), CMB-S4+LSST (orange), and CMB-S4+CSST (blue). Results are shown for 10 lens redshift bins, with violin plots representing 1σ uncertainty distributions. Annotations in the top-left report the average uncertainty $\langle\sigma(\delta b_g)\rangle$ for each survey and its percentage change relative to the SO+LSST baseline (purple). The horizontal gray dashed line marks the fiducial zero value for all bias perturbations.

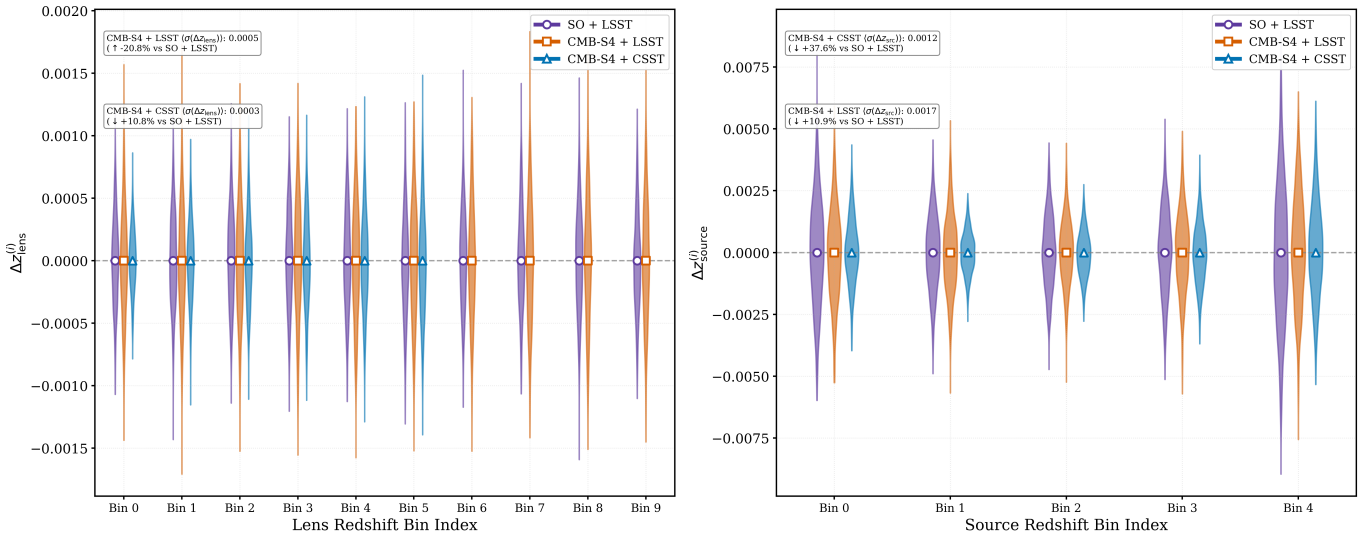


Figure 7. Constraints on photometric redshift shift nuisance parameters for tomographic survey combinations: SO+LSST (purple), CMB-S4+LSST (orange), and CMB-S4+CSST (blue). Violin plots show 1σ uncertainty distributions for each redshift bin. *Left:* Lens photo-z shifts $\Delta z_{\text{lens}}^{(i)}$ across 10 lens redshift bins. *Right:* Source photo-z shifts $\Delta z_{\text{source}}^{(i)}$ across 5 source redshift bins. Annotations in the top-left of each panel report the average uncertainty $\langle\sigma(\Delta z)\rangle$ and percentage changes relative to the SO+LSST baseline. The horizontal gray dashed lines mark the fiducial zero shift value.

- Allen, S. W., Evrard, A. E., & Mantz, A. B. 2011, *ARA&A*, 49, 409, doi: [10.1146/annurev-astro-081710-102514](https://doi.org/10.1146/annurev-astro-081710-102514)
- Arnaud, M., Pratt, G. W., Piffaretti, R., et al. 2010, *A&A*, 517, A92, doi: [10.1051/0004-6361/200913416](https://doi.org/10.1051/0004-6361/200913416)
- Asgari, M., Lin, C.-A., Joachimi, B., et al. 2021, *A&A*, 645, A104, doi: [10.1051/0004-6361/202039070](https://doi.org/10.1051/0004-6361/202039070)
- Aymerich, G., Douspis, M., Battaglia, N., et al. 2025, arXiv e-prints, arXiv:2509.08673, doi: [10.48550/arXiv.2509.08673](https://doi.org/10.48550/arXiv.2509.08673)
- Battaglia, N., Bond, J. R., Pfrommer, C., & Sievers, J. L. 2012, *ApJ*, 758, 75, doi: [10.1088/0004-637X/758/2/75](https://doi.org/10.1088/0004-637X/758/2/75)
- Bolliet, B. 2020, in *European Physical Journal Web of Conferences*, Vol. 228, mm Universe @ NIKA2 - Observing the mm Universe with the NIKA2 Camera (EDP), 00005, doi: [10.1051/epjconf/202022800005](https://doi.org/10.1051/epjconf/202022800005)
- Braspenning, J., Schaye, J., Schaller, M., Kugel, R., & Kay, S. T. 2025, *MNRAS*, 536, 3784, doi: [10.1093/mnras/stae2798](https://doi.org/10.1093/mnras/stae2798)
- Camphuis, E., Quan, W., Balkenhol, L., et al. 2025, arXiv e-prints, arXiv:2506.20707, doi: [10.48550/arXiv.2506.20707](https://doi.org/10.48550/arXiv.2506.20707)
- Chang, C., Jarvis, M., Jain, B., et al. 2013, *MNRAS*, 434, 2121, doi: [10.1093/mnras/stt1156](https://doi.org/10.1093/mnras/stt1156)
- Chisari, N. E., Alonso, D., Krause, E., et al. 2019, *ApJS*, 242, 2, doi: [10.3847/1538-4365/ab1658](https://doi.org/10.3847/1538-4365/ab1658)
- Choppin de Janvry, J., Dai, B., Gontcho, S. G. A., Seljak, U., & Zhang, T. 2025, arXiv e-prints, arXiv:2511.18134, doi: [10.48550/arXiv.2511.18134](https://doi.org/10.48550/arXiv.2511.18134)
- Cooray, A., & Sheth, R. 2002, *PhR*, 372, 1, doi: [10.1016/S0370-1573\(02\)00276-4](https://doi.org/10.1016/S0370-1573(02)00276-4)
- Corasanti, P. S., Richardson, T. R. G., Etori, S., et al. 2025, *A&A*, 697, A33, doi: [10.1051/0004-6361/202553914](https://doi.org/10.1051/0004-6361/202553914)
- CSST Collaboration, Gong, Y., Miao, H., et al. 2025, arXiv e-prints, arXiv:2507.04618, doi: [10.48550/arXiv.2507.04618](https://doi.org/10.48550/arXiv.2507.04618)
- Duffy, A. R., Schaye, J., Kay, S. T., & Dalla Vecchia, C. 2008, *MNRAS*, 390, L64, doi: [10.1111/j.1745-3933.2008.00537.x](https://doi.org/10.1111/j.1745-3933.2008.00537.x)
- Euclid Collaboration, Blanchard, A., Camera, S., et al. 2020, *A&A*, 642, A191, doi: [10.1051/0004-6361/202038071](https://doi.org/10.1051/0004-6361/202038071)
- Ferté, A., & Hong, K. 2024, *PhRvD*, 109, 103502, doi: [10.1103/PhysRevD.109.103502](https://doi.org/10.1103/PhysRevD.109.103502)
- Fumagalli, A., Costanzi, M., Castro, T., et al. 2025, arXiv e-prints, arXiv:2510.13509, doi: [10.48550/arXiv.2510.13509](https://doi.org/10.48550/arXiv.2510.13509)
- Gallardo, P. A., Puddu, R., Harrington, K., et al. 2024a, *ApOpt*, 63, 310, doi: [10.1364/AO.501744](https://doi.org/10.1364/AO.501744)
- Gallardo, P. A., Harrington, K., Puddu, R., et al. 2024b, in *Society of Photo-Optical Instrumentation Engineers (SPIE) Conference Series*, Vol. 13094, Ground-based and Airborne Telescopes X, ed. H. K. Marshall, J. Spyromilio, & T. Usuda, 130942F, doi: [10.1117/12.3020608](https://doi.org/10.1117/12.3020608)
- Gong, Y., Liu, X., Cao, Y., et al. 2019, *ApJ*, 883, 203, doi: [10.3847/1538-4357/ab391e](https://doi.org/10.3847/1538-4357/ab391e)
- Gong, Y., Miao, H., Zhou, X., et al. 2025, *Science China Physics, Mechanics, and Astronomy*, 68, 280402, doi: [10.1007/s11433-025-2646-2](https://doi.org/10.1007/s11433-025-2646-2)
- Gu, S., van Waerbeke, L., Bernardeau, F., & Dalal, R. 2025, *PhRvD*, 111, 083530, doi: [10.1103/PhysRevD.111.083530](https://doi.org/10.1103/PhysRevD.111.083530)
- Gu, S., van Waerbeke, L., Bernardeau, F., & Fabbro, S. 2026, *PhRvD*, 113, 023528, doi: [10.1103/y7c6-t42s](https://doi.org/10.1103/y7c6-t42s)
- Harnois-Déraps, J., van Waerbeke, L., Viola, M., & Heymans, C. 2015, *MNRAS*, 450, 1212, doi: [10.1093/mnras/stv646](https://doi.org/10.1093/mnras/stv646)
- Hensley, B. S., Clark, S. E., Fanfani, V., et al. 2022, *ApJ*, 929, 166, doi: [10.3847/1538-4357/ac5e36](https://doi.org/10.3847/1538-4357/ac5e36)
- Ibitoye, A., Tramonte, D., Ma, Y.-Z., & Dai, W.-M. 2022, *ApJ*, 935, 18, doi: [10.3847/1538-4357/ac7b8c](https://doi.org/10.3847/1538-4357/ac7b8c)
- Komatsu, E., & Seljak, U. 2002, *MNRAS*, 336, 1256, doi: [10.1046/j.1365-8711.2002.05889.x](https://doi.org/10.1046/j.1365-8711.2002.05889.x)
- Le Brun, A. M. C., McCarthy, I. G., & Melin, J.-B. 2015, *MNRAS*, 451, 3868, doi: [10.1093/mnras/stv1172](https://doi.org/10.1093/mnras/stv1172)
- Lewis, A., Challinor, A., & Lasenby, A. 2000, *ApJ*, 538, 473, doi: [10.1086/309179](https://doi.org/10.1086/309179)
- Limber, D. N. 1953, *ApJ*, 117, 134, doi: [10.1086/145672](https://doi.org/10.1086/145672)
- Lin, H., Gong, Y., Chen, X., et al. 2022, *MNRAS*, 515, 5743, doi: [10.1093/mnras/stac2126](https://doi.org/10.1093/mnras/stac2126)
- LSST Science Collaboration, Abell, P. A., Allison, J., et al. 2009, arXiv e-prints, arXiv:0912.0201, doi: [10.48550/arXiv.0912.0201](https://doi.org/10.48550/arXiv.0912.0201)
- Ma, Z., Hu, W., & Huterer, D. 2006, *ApJ*, 636, 21, doi: [10.1086/497068](https://doi.org/10.1086/497068)
- McCarthy, I. G., Schaye, J., Bird, S., & Le Brun, A. M. C. 2017, *MNRAS*, 465, 2936, doi: [10.1093/mnras/stw2792](https://doi.org/10.1093/mnras/stw2792)
- Mead, A. J., Brieden, S., Tröster, T., & Heymans, C. 2021, *MNRAS*, 502, 1401, doi: [10.1093/mnras/stab082](https://doi.org/10.1093/mnras/stab082)
- Miyatake, H., Battaglia, N., Hilton, M., et al. 2019, *ApJ*, 875, 63, doi: [10.3847/1538-4357/ab0af0](https://doi.org/10.3847/1538-4357/ab0af0)
- Nagai, D., Vikhlinin, A., & Kravtsov, A. V. 2007, *ApJ*, 655, 98, doi: [10.1086/509868](https://doi.org/10.1086/509868)
- Navarro, J. F., Frenk, C. S., & White, S. D. M. 1996, *ApJ*, 462, 563, doi: [10.1086/177173](https://doi.org/10.1086/177173)
- Nelson, K., Lau, E. T., & Nagai, D. 2014, *ApJ*, 792, 25, doi: [10.1088/0004-637X/792/1/25](https://doi.org/10.1088/0004-637X/792/1/25)
- Pandey, S., Gatti, M., Baxter, E., et al. 2022, *PhRvD*, 105, 123526, doi: [10.1103/PhysRevD.105.123526](https://doi.org/10.1103/PhysRevD.105.123526)

- Planck Collaboration, Ade, P. A. R., Aghanim, N., et al. 2016, *A&A*, 594, A24, doi: [10.1051/0004-6361/201525833](https://doi.org/10.1051/0004-6361/201525833)
- Planck Collaboration, Aghanim, N., Akrami, Y., et al. 2020, *A&A*, 641, A6, doi: [10.1051/0004-6361/201833910](https://doi.org/10.1051/0004-6361/201833910)
- Qu, F. J., Sherwin, B. D., Madhavacheril, M. S., et al. 2024, *ApJ*, 962, 112, doi: [10.3847/1538-4357/acfe06](https://doi.org/10.3847/1538-4357/acfe06)
- Raghunathan, S. 2022, *ApJ*, 928, 16, doi: [10.3847/1538-4357/ac510f](https://doi.org/10.3847/1538-4357/ac510f)
- Raghunathan, S., Whitehorn, N., Alvarez, M. A., et al. 2022, *ApJ*, 926, 172, doi: [10.3847/1538-4357/ac4712](https://doi.org/10.3847/1538-4357/ac4712)
- The LSST Dark Energy Science Collaboration, Mandelbaum, R., Eifler, T., et al. 2018, arXiv e-prints, arXiv:1809.01669, doi: [10.48550/arXiv.1809.01669](https://doi.org/10.48550/arXiv.1809.01669)
- Tinker, J., Kravtsov, A. V., Klypin, A., et al. 2008, *ApJ*, 688, 709, doi: [10.1086/591439](https://doi.org/10.1086/591439)
- Tinker, J. L., Robertson, B. E., Kravtsov, A. V., et al. 2010, *ApJ*, 724, 878, doi: [10.1088/0004-637X/724/2/878](https://doi.org/10.1088/0004-637X/724/2/878)
- To, C., Krause, E., Rozo, E., et al. 2021, *PhRvL*, 126, 141301, doi: [10.1103/PhysRevLett.126.141301](https://doi.org/10.1103/PhysRevLett.126.141301)
- Vikhlinin, A., Kravtsov, A. V., Burenin, R. A., et al. 2009, *ApJ*, 692, 1060, doi: [10.1088/0004-637X/692/2/1060](https://doi.org/10.1088/0004-637X/692/2/1060)
- Šarčević, N., Leonard, C. D., Rau, M. M., & the LSST Dark Energy Science Collaboration. 2025, *MNRAS*, 537, 1924, doi: [10.1093/mnras/staf156](https://doi.org/10.1093/mnras/staf156)
- Wright, A. H., Stözlner, B., Asgari, M., et al. 2025, *A&A*, 703, A158, doi: [10.1051/0004-6361/202554908](https://doi.org/10.1051/0004-6361/202554908)
- Xiong, Q., Gong, Y., Zhou, X., et al. 2025, *ApJ*, 985, 131, doi: [10.3847/1538-4357/adcb44](https://doi.org/10.3847/1538-4357/adcb44)
- Zhang, T., Li, X., Sugiyama, S., et al. 2025, arXiv e-prints, arXiv:2507.01386, doi: [10.48550/arXiv.2507.01386](https://doi.org/10.48550/arXiv.2507.01386)
- Zhang, Z. J., Chang, C., Larsen, P., et al. 2022, *MNRAS*, 514, 2181, doi: [10.1093/mnras/stac1407](https://doi.org/10.1093/mnras/stac1407)
- Zheng, Z., Berlind, A. A., Weinberg, D. H., et al. 2005, *ApJ*, 633, 791, doi: [10.1086/466510](https://doi.org/10.1086/466510)